Aerospace Science and Technology 178 (2026) 113199

Contents lists available at ScienceDirect

Aerospace Science and Technology

journal homepage: www.elsevier.com/locate/aescte

# Hydrogen-induced changes in flame topology, coherent structures, and instability development in a premixed swirl-stabilized combustor

Sara Bonuso, Pasquale Di Gloria, Guido Marseglia *, Maria Grazia De Giorgi

*Dep. of Engineering for Innovation, University of Salento, Via per Monteroni, Lecce, I-73100, Italy*

ARTICLE INFO

Communicated by: Cummings Russell

*Keywords:*
Aerospace sector
Hydrogen
Flames
Low emission
Combustion technologies
Sustainable fuels

ABSTRACT

Hydrogen is increasingly being used in the aerospace sector as a clean energy source. The premixed combustion of hydrogen–air mixtures in porous media has received considerable attention, with the aim of enhancing hydrogen energy conversion efficiency and mitigating environmental impacts.

This work experimentally investigates the influence of hydrogen enrichment on the morphology, spectral response, and temporal coherence of premixed methane–hydrogen combustion flames in a swirl-stabilized combustor at atmospheric pressure. Three fuel compositions (0%, 30%, and 40% $H_2$ by volume) were tested at constant thermal power (4.6 kW) and equivalence ratio ($\phi = 0.8$). Hydrogen addition produced more compact, intense, and symmetric CH* and OH* chemiluminescence fields, indicating increased reactivity and stronger localization of the reaction zone.

However, this morphological compactness was accompanied by a marked increase in dynamic instability. The main acoustic peaks rose from about 225 and 195 Pa at 240 and 300 Hz in the methane flame to 526 and 496 Pa at 30% $H_2$, while at 40% $H_2$ the dominant peak shifted to 310 Hz and reached 581 Pa, together with a broader spectral distribution. SPOD revealed a progressive shift from low-frequency coherent structures to fragmented higher-frequency modes, with CH* and OH* dominant frequencies extending up to 207.5 Hz at 40% $H_2$. Temporal autocorrelation further showed a transition from stable periodic behavior at 0% $H_2$ to strong mid-frequency coherence at 30% $H_2$ and rapid decorrelation at 40% $H_2$. The results demonstrate that hydrogen enrichment simultaneously enhances flame compactness and amplifies unsteady flame–acoustic interactions, defining a clear trade-off between combustion reactivity and dynamic stability.

## 1. Introduction

Hydrogen ($H_2$) is increasingly recognized as a promising energy carrier due to its ability to generate energy with zero direct carbon emissions during combustion, producing primarily water as the main by-product. This characteristic makes hydrogen a key candidate for decarbonizing both energy and transportation sectors, supporting global efforts toward net-zero emissions. In addition to its clean combustion properties, hydrogen plays a crucial role in integrated energy systems, where its production, purification, and utilization are being actively developed to improve efficiency and reduce environmental impact [1]. To meet decarbonization goals, it is shifting toward sustainable propulsion systems designed to reduce emissions, improve fuel efficiency, and integrate cleaner energy sources, making future aircraft quieter and more efficient [2,3].

Recent studies in the aviation sector have highlighted advances in hydrogen-based processes, including low-carbon combustion pathways, purification of industrial off-gases, and syngas production routes that serve as intermediates for the synthesis of sustainable aviation fuels (SAFs) and hydrogen, thereby supporting their potential integration into future aeronautical energy systems. The safety and performance aspects of hydrogen–air systems continue to be investigated to ensure reliable large-scale deployment in aviation, where SAFs are increasingly being considered [4–7]. While the long-term goal is a transition to 100% green hydrogen with minimal environmental impact, near-term strategies focus on blending hydrogen with natural gas, primarily methane, to partially decarbonize gas turbines and industrial combustion processes [8].

In this context, detailed knowledge of flame dynamics and structural properties of hydrogen as a SAF is fundamental for understanding combustion development and the associated performance [1,9–12].

Modern combustion systems emphasize "fuel flexibility," the ability

* Corresponding author.
*E-mail address:* guido.marseglia@unisalento.it (G. Marseglia).

https://doi.org/10.1016/j.ast.2026.113199
Received 2 May 2026; Received in revised form 24 June 2026; Accepted 11 July 2026
Available online 12 July 2026

to safely and efficiently operate with variable hydrogen fractions, including hydrogen carriers like ammonia [13]. Hydrogen differs from methane in terms of laminar flame speed, increasing from SL = 0.3 m/s for methane to SL = 2.5 m/s for pure $H_2$ under stoichiometric conditions [14]. Stable combustion requires the flow velocity to match the flame propagation speed; deviations can lead to upstream flame movement. While methane flames are generally stable with well-defined ignition and flammability limits, hydrogen's wide flammability range (4–75% by volume in air versus 5–15% for methane) and high diffusivity present both operational flexibility and challenges for flame stabilization [15]. Additionally, $H_2$ flames reach higher adiabatic temperatures, potentially increasing NOx emissions, although lean premixed operation can mitigate thermal NOx through reduced oxygen availability and shorter residence times [16]. Hydrogen-enriched methane blends thus offer potential advantages in reducing emissions while maintaining efficient combustion [17,18].

Several studies have investigated hydrogen addition in different burner configurations. Early work focused on dual-fuel and swirl-stabilized systems, analyzing flame stabilization, pollutant formation, and combustion dynamics. Marragou et al. [19] examined $CH_4/H_2$ dual-fuel swirl burners, while Patel et al. [20] studied hydrogen enrichment effects on swirling and non-swirling inverse diffusion flames. Kwak et al. [21] and Li et al. [22] investigated forced responses of $CH_4/H_2$ flames in dual-nozzle swirl-stabilized combustors, and An et al. [23] explored flame-shape transitions in 3D-printed low-swirl $H_2$-enriched $CH_4$/air burners. Guo et al. [24] demonstrated that hydrogen addition affects combustion intensity and radical concentration at the flame attachment in $CH_4/H_2$/air mixtures ($ZH_2$ = 0%, 40%, 80%), where $ZH_2$ represents the hydrogen volume fraction in the fuel mixture. Other works examined hydrogen-enriched flames across different scales and geometries: Wu et al. [25] studied stabilization in $H_2$-fueled reacting wall-jet flames, Kim et al. [26] investigated flame characteristics under varying swirl strengths using PIV, thermocouples, and OH chemiluminescence, and Morsy and Yang [27] analyzed instabilities in laminar $CH_4/H_2$/air flames. Yilmaz et al. [28] and Reyes et al. [29] focused on flame propagation and instabilities in $CH_4/H_2$ mixtures, while high-fidelity simulations by Xie et al. [30], Castellani et al. [31], Park et al. [32], Jejurkar et al. [33], and Cai et al. [34] examined flame stability and turbulence–reaction coupling in hydrogen-enriched flames. Pachano et al. [35] conducted numerical simulations on lean natural gas flames with varying hydrogen concentrations in a PRECCINSTA system, highlighting flame lift-off and stabilization through recirculation zones and effective fuel–air mixing under lean conditions to limit NOx emissions. Despite this extensive research, the combined spatial, spectral, and temporal effects of hydrogen enrichment under premixed and swirl-stabilized conditions remain insufficiently understood. The present work investigates flame behavior in a new burner operating under premixed methane conditions, focusing on the effects of hydrogen enrichment on flame structure and dynamics. The analysis encompasses multiple levels. First, a spatial characterization of the flame structure identifies potential changes in morphology with varying hydrogen content. Subsequently, high-frequency components [200–500 Hz] associated with the acoustic field are examined through microphone measurements to capture pressure fluctuations linked to flame–acoustic interactions. Finally, low-frequency components [15–200 Hz] are analyzed using Spectral Proper Orthogonal Decomposition (SPOD) applied to processed images of $CH_4/H_2$ flames, along with spatial autocorrelation, to isolate coherent structures and dominant energetic modes within the flame. This integrated approach enables the identification of how hydrogen enrichment modifies the flame's compactness, symmetry, and dynamic stability, providing insights into the interplay between enhanced chemical reactivity, turbulence, and thermoacoustic feedback.

Hydrogen's high diffusivity and low Lewis number promote faster flame propagation and preferential diffusion effects, leading to increased flame-front wrinkling and radical production. Consequently, hydrogen addition affects both flame stabilization and the formation of coherent structures, impacting oscillatory behaviors and instabilities across multiple frequency ranges. By combining spatial, spectral, and temporal analyses, the study offers a comprehensive understanding of the effects of hydrogen enrichment, addressing gaps in the literature regarding partially premixed, swirl-stabilized flames. This work contributes to optimizing hydrogen–methane combustion in practical applications, enhancing flame stability, efficiency, and control while supporting the broader transition toward low-carbon energy solutions.

The rationale of the present study is to clarify how hydrogen enrichment modifies not only the mean topology of premixed methane flames, but also their spectral response, coherent structures, and instability development in a swirl-stabilized combustor. While previous studies have addressed individual aspects such as flame stabilization, emissions, global chemiluminescence, or numerical flame stability, a combined analysis integrating CH*/OH* chemiluminescence imaging, geometrical flame descriptors, acoustic measurements, SPOD-based modal decomposition, and autocorrelation analysis remains limited. The objective of this work is therefore to provide an integrated experimental characterization of the spatial, spectral, and temporal effects induced by hydrogen enrichment in methane–hydrogen swirl-stabilized flames.

## 2. Materials and methods

This section details the experimental setup and methodology used to investigate flame dynamics in premixed methane–hydrogen combustion, with a focus on identifying the mechanisms driving pressure oscillations and low-frequency instabilities.

Section 2.1 provides a detailed description of the experimental setup, including the combustion chamber, the fuel supply and mixing system, and the equipment used for both acoustic and optical measurements. Section 2.2 focuses on the application of high-speed chemiluminescence imaging to visualize the emissions of reactive radicals (CH* and OH*). It also introduces the use of Zernike moments and Hu invariant moments, which are useful for analyzing the topology and symmetry of the flame under various operating conditions. Zernike moments provide a compact mathematical description of flame shape by decomposing the image into orthogonal spatial patterns. Higher-order moments are associated with increasingly complex geometric features and asymmetries. Hu invariant moments are shape descriptors that remain unchanged under translation, rotation, and scaling, making them particularly useful for comparing flame structures under different operating conditions.

Section 2.3 introduces the Spectral Proper Orthogonal Decomposition (SPOD) method, a modal decomposition technique employed to identify dominant spectrally coherent structures within the image sequences, thereby allowing the characterization of the prevailing instability modes. Unlike conventional POD, SPOD identifies coherent structures associated with specific frequencies, enabling the investigation of frequency-dependent flame dynamics and instability mechanisms. Finally, Section 2.4 is dedicated to the analysis of acoustic signals acquired via microphones, with the aim of identifying dominant frequencies in the system and correlating them with the dynamic phenomena observed optically. The autocorrelation function quantifies the temporal persistence of flame structures by measuring the similarity of a signal with itself at different time delays.

### 2.1. Experimental setup

Flame stabilization under varying hydrogen enrichment levels was investigated using an atmospheric-pressure swirl-stabilized burner. The system comprises a central injector mounted on a support nozzle and a quartz-windowed combustion chamber (105 × 360 mm) that enables high-resolution optical diagnostics. A single burner configuration ensured the formation of an attached flame, as shown in Fig. 1a.

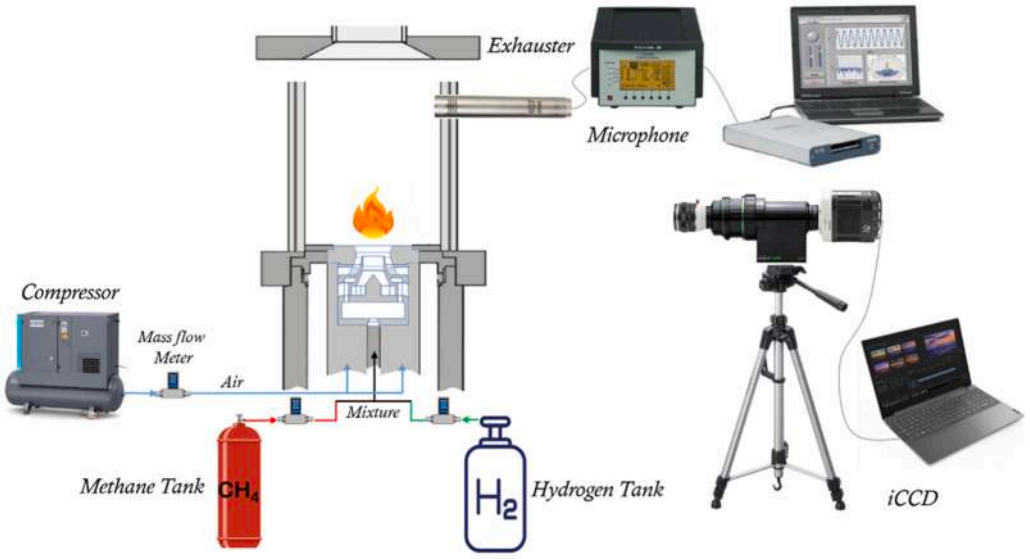


**Fig. 1a.** Experimental Set-Up.

Swirled flames were generated using an air-blast nozzle with an effective outlet area of 319 mm$^2$, representative of the geometrical scale of aero-engine combustors, similar to the configuration investigated by Kasabov et al. [36]. The nozzle assembly includes two concentric air swirlers: Swirler 1 with a geometric swirl number of 0.76 and Swirler 2 with a swirl number of 0, followed by an air diffuser. Methane and hydrogen are injected axially through a central tube, while the primary and secondary air flows are supplied through distinct inlets in the lower and upper sections of the nozzle holder (see Fig. 1b). Since Swirler 2 does not impart angular momentum to the flow, its role should be interpreted as part of the fuel/air injection and mixing arrangement rather than as an active swirl-generating element.

Experiments were conducted at an inlet air temperature of 298 K. To ensure a constant thermal power output of 4.6 kW and a fixed equivalence ratio of $\phi = 0.8$, the fuel and air flow rates were adjusted accordingly for each test case. Three fuel mixtures were investigated: pure methane and two methane–hydrogen blends with increasing hydrogen content. The complete set of operating conditions is summarized in Table 1.

For each hydrogen-enrichment condition, the methane and hydrogen flow rates were adjusted to maintain an approximately constant thermal power of 4.6 kW, while the air flow rate was kept fixed at 100 l/min. As a result, the equivalence ratio remained close to the nominal lean value of $\varphi = 0.8$, with slight variations among the investigated cases.

**Table 1**
Experimental Conditions.

| Case | $H_2$ vol [%] | Thermal Power [kW] ($P_{H2}$ Thermal Power [%]) | $CH_4$ [l/min] | $H_2$ [l/min] | Air [l/min] | φ |
|---|---|---|---|---|---|---|
| 1 | 0% | 4.6 (0%) | 8.33 | 0 | 100 | 0.793 |
| 2 | 30% | 4.6 (~51%) | 7.33 | 3.33 | 100 | 0.777 |
| 3 | 40% | 4.6 (~62%) | 6.85 | 5 | 100 | 0.771 |

For the operating conditions investigated here, a mean air bulk velocity of approximately 5.22 m/s was estimated for all operating conditions and the bulk Reynolds number based on the effective outlet area and equivalent nozzle diameter is approximately ($7.2 \times 10^3$).

Methane and hydrogen were injected axially through the central fuel tube. the estimated total fuel injection velocities are approximately 0.90 m/s for the pure methane case, 1.15 m/s for the 30% $H_2$ case, and 1.28 m/s for the 40% $H_2$ case.

Acoustic pressure signals were recorded simultaneously using a Bruel & Kjaer microphone (model 4189 A 021), positioned at a height of 39 cm

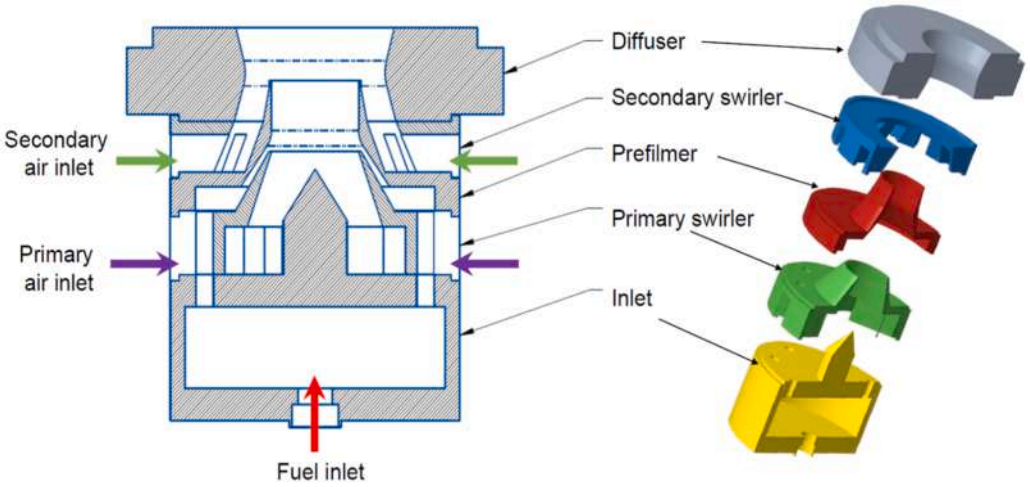


**Fig. 1b.** Zoomed-in view of the burner central region showing the air and fuel flow paths.

from the burner outlet and at a radial distance from the burner center of 11 cm, ensuring optimal sensitivity to pressure fluctuations originating from flame–acoustic interactions. The microphones were positioned at a radial distance of 11 cm from the burner axis (approximately 4.1 times the burner outlet diameter, D = 27 mm). The signals were acquired via a National Instruments NI-9324 data acquisition module at a sampling rate of 25 kHz, controlled through LabVIEW software. Microphone calibration was performed using a reference acoustic source. All acoustic data were post-processed in MATLAB®, including background noise subtraction and frequency-domain analysis.

### 2.2. High-speed chemiluminescence imaging

High-speed chemiluminescence imaging was employed to investigate flame structure by capturing CH* (431 nm) and OH* (307.1 nm) emissions, which indicate different combustion zones. CH* marks the inner reaction zone and main heat release, while OH* corresponds to high-temperature oxidation in the outer flame front [37,38].

The imaging setup consisted of a high-speed CCD camera (Phantom M320S), a UV lens (Nikon F/105 mm, f/4.5), a Lambert-type image intensifier, and two band-pass filters centered at 431 nm (CH*) and 307.1 nm (OH*). Images were acquired at 1000 Hz to capture transient flame behavior under unsteady conditions, such as those induced by swirl and hydrogen enrichment.

For each test case, time-averaged (mean) and fluctuating (variance) fields were extracted. The mean image highlights the global flame shape, while the variance reveals regions of instability linked to flame wrinkling, vortex shedding, or local extinction/reignition.

To assess flame topology and symmetry, Zernike moments and Hu invariant moments were computed. Zernike moments are obtained by projecting the image function $f(x,y)$ onto a set of orthogonal polynomials:

$$Z_{nm} = \frac{n+1}{\pi} \iint_{x^2+y^2 \le 1} f(x,y) V^*_{nm}(x,y) dxdy \tag{1}$$

where $V_{nm}(x,y)$ are Zernike polynomials. Their magnitudes $|Z_{nm}|$ represent the strength of specific shape features—useful for analyzing flame asymmetry, curvature, and fragmentation [39,40]. They are invariant to rotation, and normalization ensures scale and translation invariance. Lower-order moments capture global shape; higher-order terms reveal localized variations.

Hu moments, based on normalized central moments $\mu_{pq}$, offer an alternative set of rotation-, scale- and translation-invariant descriptors:

$$\eta_{pq} = \frac{\mu_{pq}}{\mu_{00}^{\left(1+\frac{p+q}{2}\right)}} \tag{2}$$

The seven Hu invariants $\phi_1,\ldots,\phi_7$ are nonlinear combinations of these terms [41,42]. They are particularly useful for distinguishing subtle differences in flame symmetry and deformation and are robust to noise.

Together, these descriptors offer a compact, quantitative framework to assess how hydrogen enrichment alters flame morphology and dynamics.

### 2.3. Spectral proper orthogonal decomposition (SPOD)

To investigate coherent spatio-temporal structures in the reacting flow, Spectral Proper Orthogonal Decomposition (SPOD) was applied to time-resolved chemiluminescence image sequences. SPOD is a dynamic technique that decomposes the fluctuating component of a scalar or vector field into orthogonal modes that are both temporally harmonic and spatially correlated. Unlike classical Proper Orthogonal Decomposition (POD), which is optimal in a time-averaged energy sense, SPOD yields a frequency-dependent basis, allowing energetic structures oscillating at distinct frequencies to be isolated [43]. Let $q(x,t)$ be the zero-mean fluctuating component of the measured signal (e.g., CH* or OH* intensity at each pixel). The signal is segmented into overlapping windows, and the Fourier transform is computed within each segment using the Welch method [44], enhancing statistical convergence. For each frequency $f$, the cross-spectral density (CSD) matrix is computed as:

$$S(f) = E[q(f)q^*(f)] \tag{3}$$

where $q(f)$ is the discrete Fourier transform in each window, $q^*(f)$ its Hermitian transpose, and $E$ denotes ensemble averaging. SPOD modes are obtained by solving:

$$S(f)\Phi_k(f) = \lambda_k(f)\Phi_k(f) \tag{4}$$

where $\Phi_k$ represents the $k$-*th* SPOD mode at frequency $f$, and $\lambda_k(f)$ its energy. Modes are orthogonal and ordered $\lambda_1(f) \ge \lambda_2(f) \ge \ldots$, highlighting dominant structures per frequency.

Each mode $\Phi_k(f)$ captures a spatial oscillation at frequency $f$, while $\lambda_k(f)$ quantifies its energetic relevance. SPOD is well suited for detecting combustion instabilities, thermoacoustic modes, and shear-driven oscillation in turbulent flames [45,46]. In practice, high-speed chemiluminescence videos are reshaped into 2D matrices (space × time). A Fourier transform is applied along the time axis, and SPOD is performed for each frequency bin. This frequency-resolved method effectively separates coherent flame dynamics from turbulent noise and allows direct comparison with time-resolved acoustic data. Building on this, the analysis continues with high-frequency [200–500 Hz] acoustic emissions recorded by microphones, essential for identifying pressure-driven instabilities and flame–acoustic coupling.

### 2.4. Acoustic signal analysis

Prior to spectral analysis, the acoustic signals underwent preprocessing steps to remove electrical background noise and compensate for microphone sensitivity through a calibration function derived from reference sound sources.

The Power Spectral Density (PSD) of the pressure signal was computed using the Welch method [47], a widely adopted spectral estimation technique that enhances statistical reliability by averaging multiple overlapping segments of the signal. Specifically, the method divides the time series $x(t)$ into $L$ overlapping windows $x_i(t)$, applies a tapering function $w_i(t)$ (typically a Hanning window to reduce spectral leakage), and performs a Fourier transform on each segment. The PSD is then estimated as:

$$P_{XX}(f) = \frac{1}{L}\sum_{i=1}^{L} |F\{w_i(t)x_i(t)\}|^2 \tag{5}$$

where $F\{\cdot\}$ denotes the Fourier transform operator. This averaging process significantly reduces the variance of the spectral estimate, yielding a smoother and more reliable frequency spectrum (Welch, 1967).

The Welch method is particularly effective in combustion studies for isolating distinct frequency bands associated with physical phenomena such as thermoacoustic instabilities, shear-layer instabilities, and broadband turbulence-induced noise [48,49]. In this work, the technique facilitated the identification of high-frequency spectral peaks linked to flame-acoustic coupling and provided a quantitative assessment of how hydrogen enrichment influences the noise signature of the burner.

#### 2.4.1. Frequency-domain analysis of pressure signals

The frequency domain analysis presented in Fig. 2 highlights the evolution of the acoustic spectrum as hydrogen is added to the methane-air mixture. While low-frequency peaks remain consistently prominent across all conditions, the behavior at higher frequencies reveals notable

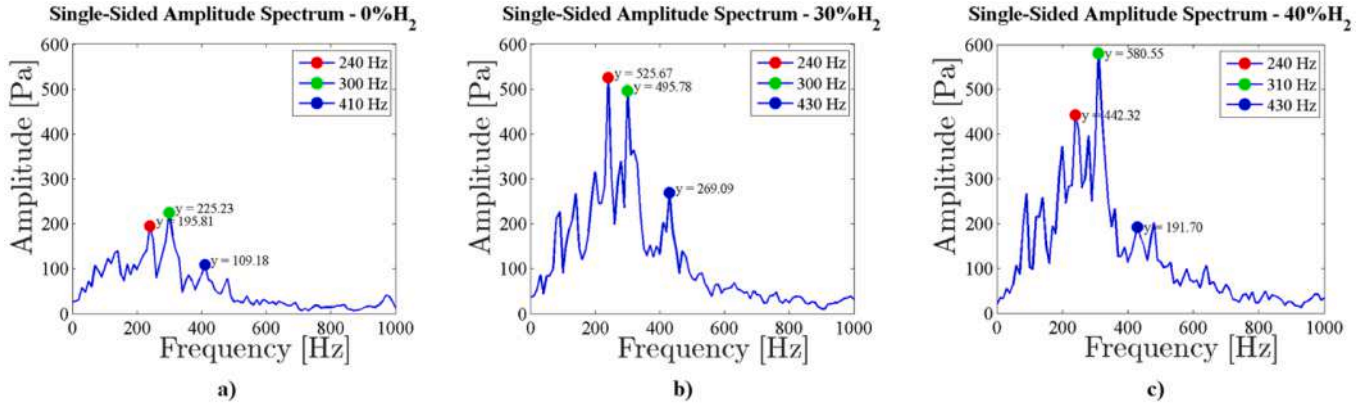


**Fig. 2.** Single-sided amplitude spectra of the pressure signal for increasing hydrogen enrichment (a) 0% $H_2$, (b) 30% $H_2$, (c) 40% $H_2$.

trends with hydrogen enrichment (fluctuations in the frequency range between 46.88 and 93.75).

At 0% $H_2$ (Fig. 2a), the spectrum is characterized by three distinct peaks located at approximately 240 Hz, 300 Hz, and 410 Hz, with amplitudes of about 225 Pa, 195 Pa, and 109 Pa, respectively. These peaks suggest the presence of moderate acoustic instabilities, possibly linked to combustion-driven pressure oscillations inherent to the system geometry and the flame dynamics. Although these pressure amplitudes are lower than those observed for the hydrogen-enriched cases, the interpretation of comparatively weak flame–acoustic coupling is strengthened when the acoustic data are considered together with the optical diagnostics.

This interpretation is further supported by the comparison with the optical diagnostics, as discussed in the spectral-energy analysis of pressure, CH*, and OH* signals in the next section. The normalized spectral-energy analysis shows that the pressure response is mainly concentrated in the 150–300 Hz band, whereas the CH* and OH* POD modes are dominated by lower-frequency flame-structure dynamics. For the 0% $H_2$ case, the acoustic peaks are therefore not accompanied by a comparable broadening of the chemiluminescence spectra, suggesting limited coupling between unsteady heat release and the acoustic field. Conversely, with hydrogen enrichment, the increase in pressure amplitude is accompanied by stronger CH*/OH* fluctuation localization and broader optical spectral content, indicating a progressive strengthening of flame–acoustic interaction.

With the introduction of 30% $H_2$ (Fig. 2b), there is a substantial increase in the amplitude of the first two peaks. The peaks at 240 Hz and 300 Hz reach amplitudes of approximately 526 Pa and 496 Pa, respectively more than doubling compared to the baseline case. This implies a strong flame-acoustic coupling, likely due to the increased reactivity and heat release rate induced by hydrogen. The third peak at 430 Hz also becomes more pronounced (~269 Pa), indicating a broader excitation of higher modes.

At 40% $H_2$ (Fig. 2c), the general structure of the spectrum remains similar, but with notable shifts. The second peak slightly shifts to 310 Hz and further increases in amplitude to about 581 Pa, now becoming the dominant component in the spectrum. The first peak at 240 Hz slightly decreases to 442 Pa, while the third peak at 430 Hz reduces in amplitude to ~192 Pa. This suggests a redistribution of energy in the frequency domain and possibly a shift in the dominant instability mechanism. The persistence of high-energy content across multiple peaks confirms a sustained interaction between combustion dynamics and the acoustic field.

These findings indicate that hydrogen enrichment amplifies acoustic instabilities, particularly in the low-to-mid frequency range (240–310 Hz) and broadens the spectrum by enhancing higher-frequency components. This is consistent with a more energetic and reactive flame, whose faster kinetics and shorter reaction zones act as more effective sources of unsteady heat release, thereby exciting a wider range of acoustic modes.

## 3. Flame structure, dynamics, and modal analysis

This section outlines the experimental and analytical methods employed to investigate thermoacoustic instabilities and flame dynamics in premixed methane–hydrogen combustion. Optical and acoustic diagnostics were used to characterize CH* and OH* radical emissions, corresponding to heat release zones and high-temperature post-flame regions, respectively. In Section 3.1, high-speed CH and OH chemiluminescence imaging was performed to investigate the spatial distribution and temporal evolution of the flame. The data were subsequently processed for spatial analysis of emission patterns (Section 3.1.1) to identify active heat release and oxidation regions, and for geometrical and morphological analysis (Section 3.1.2) to quantify variations in flame structure and symmetry with fuel composition. To investigate oscillatory mechanisms and dominant instability components, a frequency-domain analysis was conducted in Section 3.2 on both acoustic and optical signals. High-frequency behavior [200–450 Hz] was analyzed via microphone measurements to detect peaks associated with acoustic or thermoacoustic modes. Low-frequency dynamics [15–200 Hz] were examined using Spectral Proper Orthogonal Decomposition (SPOD) applied to chemiluminescence images, isolating coherent structures and dominant instability modes. Finally, Section 3.3 presents the computation of autocorrelation functions to evaluate the temporal persistence of fluctuations and the presence of cyclic or chaotic flame behavior.

### 3.1. *CH* and OH* emissions*

#### 3.1.1. *Spatial analysis*

Fig. 3 illustrates the spatial distribution of CH* and OH* emissions for hydrogen concentrations of 0%, 30%, and 40% $H_2$. The flame exhibited a largely axisymmetric mean structure under all investigated operating conditions. Therefore, the regions shown in Fig. 3 correspond to equivalent sides of the flame.

To enable direct comparison, chemiluminescence images were normalized to their maximum intensity, with each image composed of two halves: one representing the hydrogen-enriched mixture and the other pure methane. This normalization preserved the relative spatial distribution, allowing a consistent analysis of the effects induced by hydrogen addition.

Hydrogen markedly alters flame structure: at 30% and 40% $H_2$, CH* intensity increases and becomes more localized (Fig. 3**a**, 3**c**), indicating a more reactive and compact flame. In contrast, at 0% $H_2$, CH* emission is more diffused. With 40% $H_2$, the CH* zone shifts downward, reflecting enhanced flame propagation due to increased laminar flame speed and

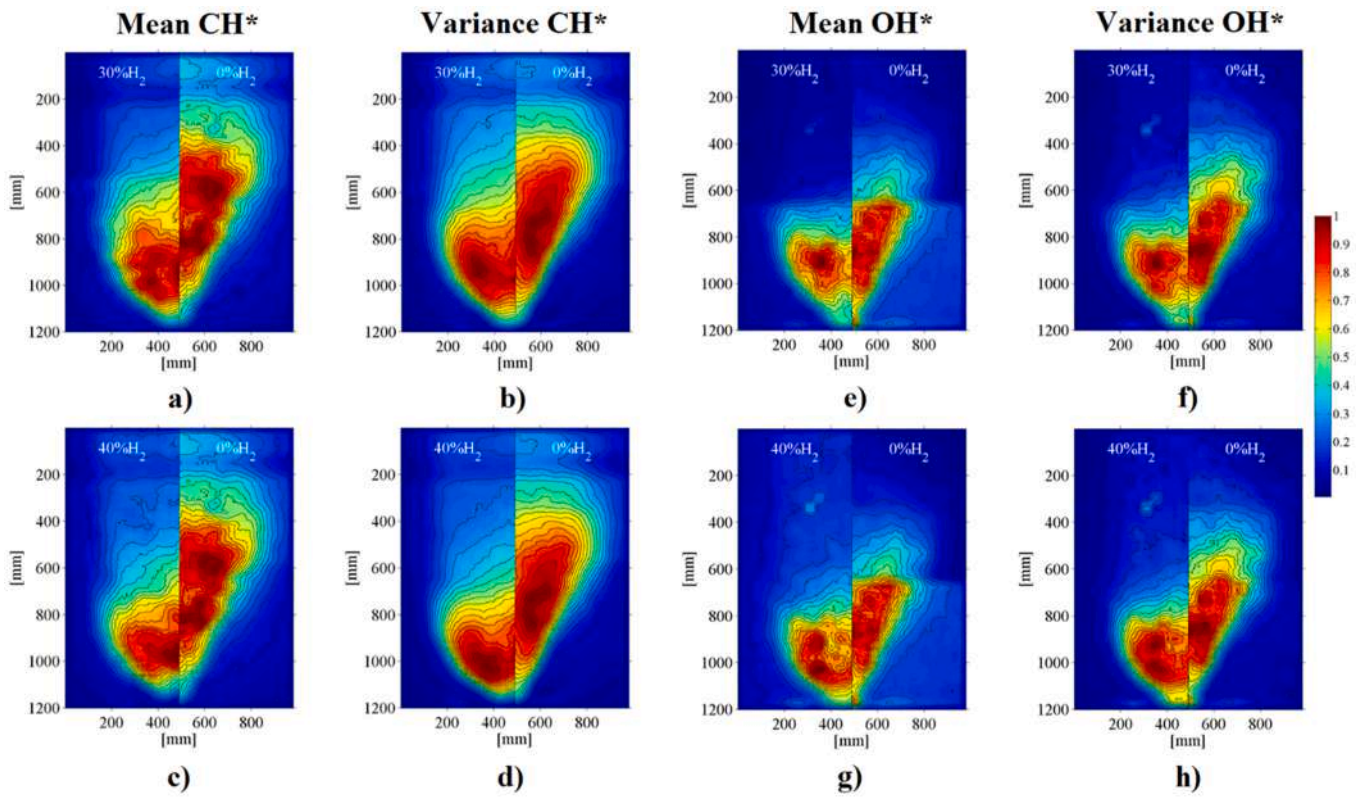


**Fig. 3.** Chemiluminescence imaging of CH* (a–d) and OH* (e–h) signals, reported as mean and variance fields. The left half of each panel corresponds to hydrogen-enriched flames (30% $H_2$ in a–b, e–f; 40% $H_2$ in c–d, g–h), while the right half represents the baseline flame without hydrogen addition (0% $H_2$).

higher radical concentrations (e.g., H, O, OH), which accelerate chain-branching reactions and stabilize the flame closer to the burner.

While the overall CH* variance patterns (Fig. 3b, 3d) remain qualitatively similar among the investigated conditions, hydrogen enrichment tends to modify the spatial distribution of variance within the central flame region. Therefore, the observed effect should be interpreted as a localized redistribution of the fluctuating CH* chemiluminescence signal rather than as a uniform increase in variance over the entire flame field. This redistribution may be associated with the higher diffusivity of hydrogen and preferential-diffusion effects, which can promote localized flame-front wrinkling and enhanced reaction-zone dynamics under lean conditions.

Similarly, the OH* mean intensity increases with hydrogen enrichment, particularly in the flame center (Fig. 3e, 3*g*), reflecting faster oxidation kinetics and enhanced OH radical production in hydrogen-enriched flames. In the baseline methane case, the OH* emission appears more distributed downstream, suggesting a slower and more spatially extended oxidation region. The OH* variance fields (Fig. 3f, 3h) also indicate a redistribution of fluctuations toward regions of higher mean intensity under hydrogen-enriched conditions, especially at 40% $H_2$. This behavior is consistent with more localized unsteady reaction-rate activity, although it should be interpreted qualitatively from the present images.

Overall, hydrogen enrichment promotes more compact and intense CH* and OH* chemiluminescence fields, while the variance maps suggest a more localized dynamic activity of the reaction zone. These effects can be related to the coupling between heat release, turbulence, and thermo-diffusive mechanisms. In particular, hydrogen's higher laminar flame speed and diffusivity may enhance preferential diffusion in lean mixtures, promoting localized flame-front wrinkling and increased radical production, as reflected in the chemiluminescence fields.

The spectral energy balance of reacting flows expresses the variance increase as:

$$\frac{\partial q'^2}{\partial t} \approx P - D + T \tag{6}$$

where $\frac{\partial q'^2}{\partial t}$ represents heat release variance, $P$ the production from turbulent–flame interaction, $D$ the dissipation, and $T$ the transport. Hydrogen enrichment increases $P$ because stronger heat release fluctuations are more efficiently coupled with the unsteady velocity field. Thermo-diffusive instability is also promoted due to hydrogen's low Lewis number, with the stability criterion given:

$$\Lambda = \frac{L_e - 1}{\phi} \tag{7}$$

where $L_e$ is the Lewis number and $\phi$ the equivalence ratio. For $H_2$–air mixtures, $L_e \ll 1$, yielding $\Lambda < 0$, which promotes cellular growth structures and amplifies flame-front fluctuations.

### 3.1.2. Geometrical and morphological analysis

Fig. 4 presents a quantitative analysis of the spatial features of CH* and OH* emissions for different hydrogen enrichment levels (0%, 30%, and 40% $H_2$), based on shape descriptors such as Zernike and Hu moments, mean curvature, area, perimeter, and centroid coordinates. These metrics complement the intensity and variance maps in Fig. 3, providing a detailed characterization of how flame structures evolve with increasing hydrogen content. For CH* emissions (Fig. 4a), the analysis reveals that the flame geometry changes significantly as hydrogen is added. With pure methane (0% $H_2$), the CH* emission zone exhibits pronounced contributions from high-order Zernike moments (Z60–Z77) and Hu moments (Hu3–Hu7), indicating an elongated, irregular, and asymmetric shape. High perimeter and area values support the observation of a diffused and extended reaction zone, consistent with the mean intensity maps in Fig. 3a. The addition of 30% hydrogen leads to a marked reduction in these higher-order moments, indicating a more

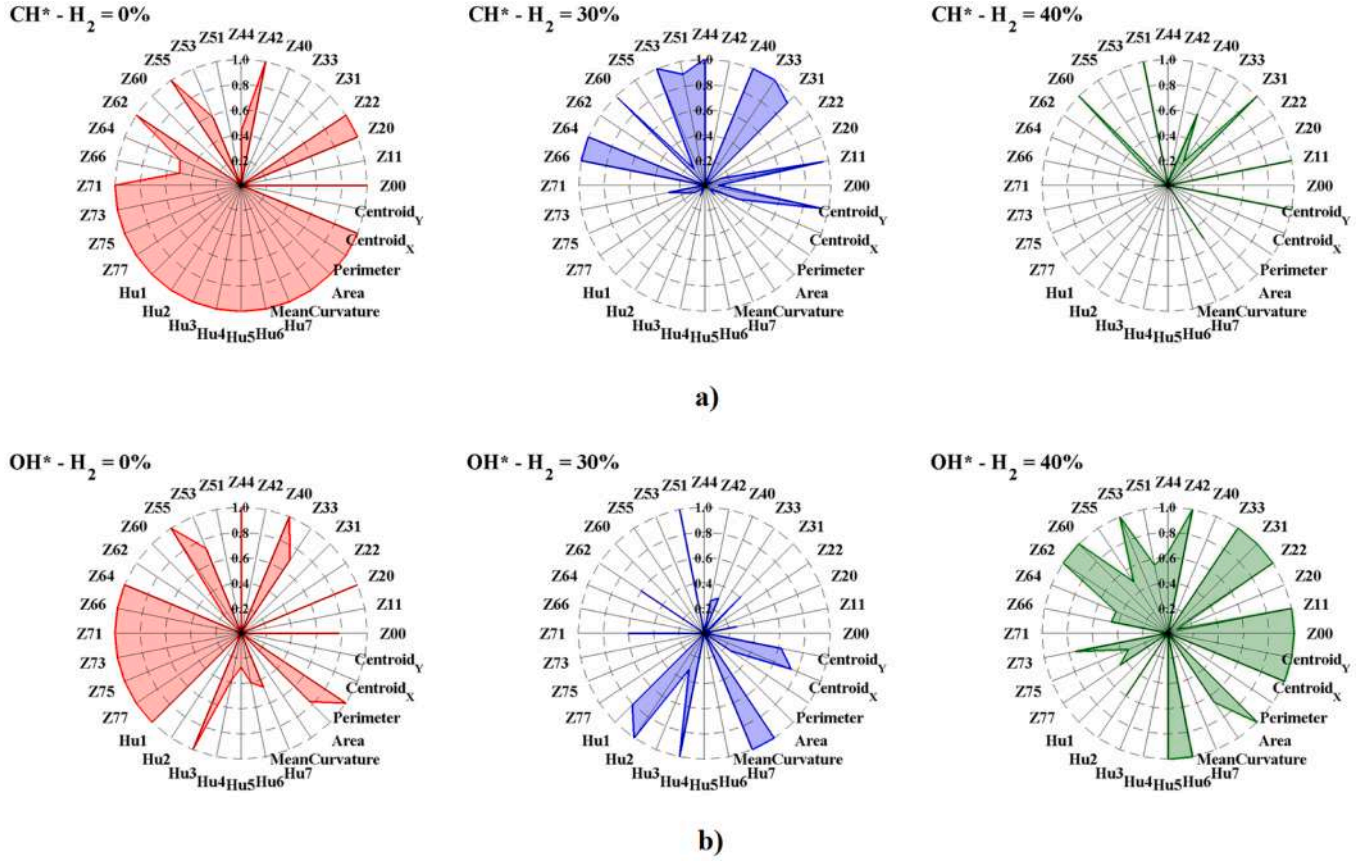


**Fig. 4.** Radar plots of normalized shape descriptors for CH* (a) and OH* (b) emissions at 0%, 30%, and 40% $H_2$.

compact and symmetric flame. The centroid shifts downward, suggesting a stabilization effect, while the reduction in area and perimeter reflects a more confined reaction region, aligning with the concentration of CH* emission observed in Fig. 3a. At 40% hydrogen, the trend continues, with minimal contributions from higher-order Zernike and Hu moments, indicating a highly symmetric and compact CH* zone. The further decrease in area and perimeter confirms stronger flame contraction and enhanced combustion efficiency, consistent with the highest CH* intensity localized in a well-defined region (Fig. 3**c**). In general, hydrogen enrichment reduces spatial complexity, progressively shifting the CH* emission toward a compact and symmetric structure, despite stronger local fluctuation levels.

A similar behavior is observed for OH* emissions (Fig. 4b). With pure methane, OH* zones exhibit high-order Zernike and Hu moments, reflecting elongated and irregular flame shapes with pronounced asymmetry, as indicated by the large perimeter and area. This aligns with the dispersed OH* distribution in Fig. 3e. The addition of 30% hydrogen reduces higher-order moments, producing a more symmetric and concentrated OH* zone. The centroid shift and decrease in area and perimeter indicate a stabilization of the reaction front, consistent with hydrogen-enhanced oxidation and reduced flame front distortions. At 40% hydrogen, the OH* emission becomes even more compact and symmetric, with minimal high-order moments and drastically reduced area and perimeter, confirming that oxidation reactions occur in a localized and intense region (Fig. 3*g*). This demonstrates that hydrogen accelerates reaction rates and increases combustion efficiency.

Comparing CH* and OH* trends reveal consistent behavior: hydrogen enrichment promotes more compact, symmetric, and intense reaction zones. These observations complement the intensity and variance results from Fig. 3, indicating that hydrogen reduces the geometric complexity of the flame while simultaneously amplifying fluctuation intensity. In this sense, hydrogen produces a flame that is morphologically ordered but dynamically more active. The reduction in geometric irregularities therefore correlates with stronger and more localized chemiluminescence, whereas the increase in variance reflects enhanced local instabilities associated with turbulence–flame interaction and thermo-diffusive effects.

Overall, the geometrical descriptors consistently indicate that hydrogen enrichment reduces flame-shape complexity and promotes a more localized reaction zone. The progressive decrease in higher-order Zernike and Hu moments, together with the reduction in area and perimeter, reflects the transition toward a more compact and symmetric flame structure. These observations suggest that hydrogen significantly modifies flame morphology and reaction dynamics, promoting a more organized reaction zone while enhancing combustion intensity. The shape-descriptor analysis therefore complements the intensity and variance maps, providing a quantitative assessment of the influence of hydrogen enrichment on flame structure and behavior.

### 3.2. *Frequency-domain analysis: acoustic and optical signals*

Understanding the dominant instability mechanisms is crucial for interpreting the thermoacoustic behavior of hydrogen-enriched premixed flames. Therefore, Spectral Proper Orthogonal Decomposition (SPOD) is applied to investigate the spatial and spectral characteristics of the coherent structures associated with flame dynamics and pressure fluctuations under different hydrogen concentrations.

Among the most effective techniques for extracting coherent structures from spatiotemporal data, SPOD stands out for its ability to identify spatial modes associated with specific frequencies. Unlike classical POD, which maximizes global energy while mixing contributions from different frequencies, SPOD enables a natural frequency separation, making it particularly suitable for the analysis of cyclic and oscillatory phenomena such as those observed in unstable flames [50].

While POD and SPOD are based on similar decomposition principles, the two methods provide complementary information. POD extracts the most energetic structures irrespective of frequency, whereas SPOD isolates coherent structures associated with specific spectral components.

The classification of the dominant frequency bands was based on previous studies on swirl-stabilized premixed flames and thermoacoustic systems. Therefore, the proposed interpretation should be regarded as a physically informed attribution supported by literature evidence rather than a direct identification of the underlying instability mechanisms [51–54].

In the present study, the SPOD-based frequency bands are interpreted only within the low-frequency range resolved by the chemiluminescence-based modal analysis. Low-frequency modes (15.63–31.25 Hz) are mainly associated with large-scale flame motion and hydrodynamic structures; intermediate-frequency modes (31.25–62.50 Hz) are interpreted as flame–flow interaction and flame-front oscillation mechanisms; and the upper SPOD band (62.50–93.75 Hz) is discussed as higher-frequency flame-structure dynamics within the optical SPOD range.

In combustion applications, applying SPOD to optical diagnostics such as chemiluminescence imaging allows dominant modes associated with flame dynamics, vortex formation, and flame–acoustic interaction to be identified. This approach provides a clearer physical interpretation of instability mechanisms and offers valuable insight for the development of active combustion control strategies.

The frequency spectrum of the first SPOD mode and the corresponding spatial structures in three frequency bands, extracted from CH* images of a premixed flame fueled with pure methane (0% $H_2$), are reported in Fig. 5. Dominant frequencies at 10, 22.5, 47.5, 60, and 80 Hz reveal recurrent spatiotemporal patterns. SPOD maps in the 15.63–31.25 Hz, 46.88–62.5 Hz, and 78.13–93.75 Hz ranges highlight coherent oscillatory features. The lowest-frequency band is associated with hydrodynamic instabilities, such as lateral oscillations and vortex shedding, while the intermediate band suggests a hybrid regime characterized by the onset of thermoacoustic coupling. The highest-frequency range exhibits more compact and symmetric structures, likely related to weak acoustic modes.

Results for combustion of a methane mixture enriched with 30% hydrogen are shown in Fig. 6. The spectrum exhibits peaks at 15, 25, 45, 67.5, and 90 Hz, with a noticeably higher contribution of high-frequency components compared to the pure methane case. The corresponding SPOD structures indicate hydrodynamic instabilities in the 15.63–31.25 Hz range, localized flame–acoustic coupling between 31.25 and 46.88 Hz, and more compact thermoacoustic modes in the 62.5–78.13 Hz and 78.13–93.75 Hz bands. Hydrogen addition therefore increases spectral complexity and spatial fragmentation, reflecting enhanced reactivity and stronger flame–acoustic interactions.

The behavior of the $CH_4/H_2$ (60/40 vol%) fuel blend is illustrated in Fig. 7. Spectral peaks are distributed over a much broader frequency range, with maxima at 25, 55, 90, 150, and 207.5 Hz, indicating a more unstable dynamics rich in harmonics. The SPOD maps reveal structures associated with hydrodynamic instabilities (15.63–31.25 Hz), flow–flame interactions (46.88–62.5 Hz), and localized acoustic modes (78.13–93.75 Hz). At higher frequencies (140.63–156.25 Hz and 203.13–218.75 Hz), compact structures emerge that are absent in the lower-hydrogen cases, possibly related to higher-order acoustic modes or modulated turbulence. The introduction of 40% hydrogen thus significantly increases the spectral complexity of the flame, shifting a portion of the modal energy toward higher frequencies and more fragmented spatial structures. The modal features extracted from CH* chemiluminescence provide a direct representation of localized heat-release regions, which are strongly influenced by the increased reactivity and higher flame propagation speed induced by hydrogen enrichment. The upper-frequency components observed in Fig. 7 should therefore be interpreted as higher-frequency flame-structure dynamics within the optical POD/SPOD range. Their possible connection with acoustic or thermoacoustic phenomena is discussed only qualitatively and in conjunction with the independently measured pressure spectra.

Based on OH* images, Fig. 8 highlights spectral peaks between 30 and 60 Hz, with a maximum around 30 Hz, indicating the presence of coherent phenomena in the post-flame region. The SPOD structures show slow oscillations at the flame base (15.63–31.25 Hz), convective instabilities (31.25–46.88 Hz), and localized oscillatory modes (46.88–62.5 Hz), albeit with low energy content ($\lambda = 0.0019$).

An increase in spectral energy relative to the hydrogen-free case is observed in Fig. 9, corresponding to OH* images at 30% $H_2$. Peaks appear at 10, 45, 52.5, 72.5, and 92.5 Hz. The associated SPOD structures reveal radial oscillations (31.25–46.88 Hz), compact vortical patterns (46.88–62.5 Hz), and extended symmetric modes (62.5–93.75 Hz), indicative of effective coupling between heat release and acoustic waves.

Further enrichment to 40% $H_2$ leads to an additional increase in

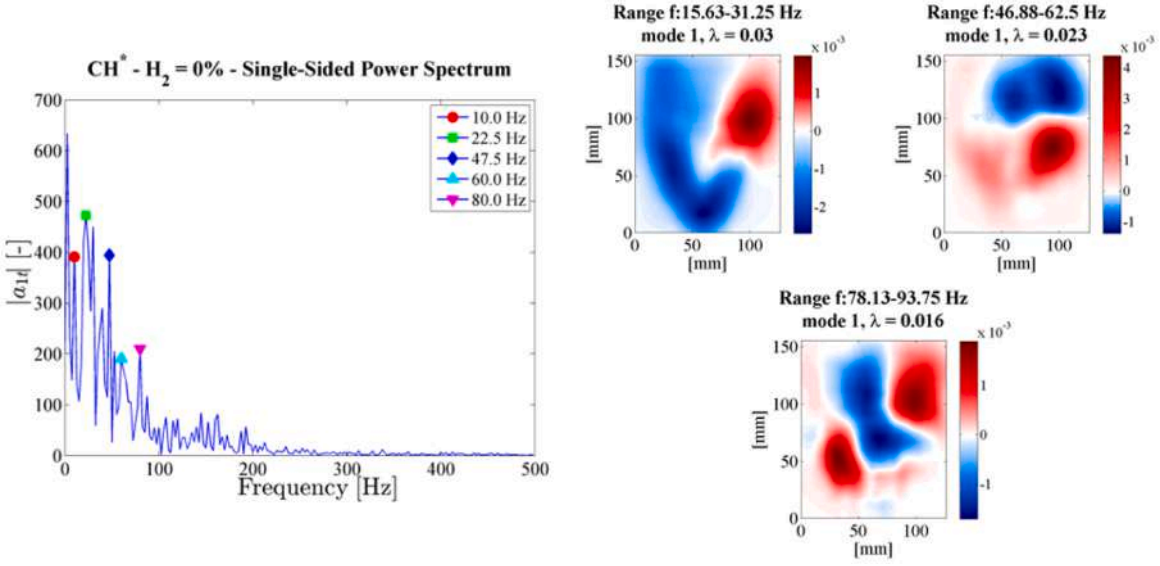


**Fig. 5.** FFT of the first mode extracted from the temporal coefficients of the POD (on the left) and flame structures of the first mode associated with frequency ranges selected through SPOD (on the right) - Chemiluminescence images of CH* with 0% $H_2$.

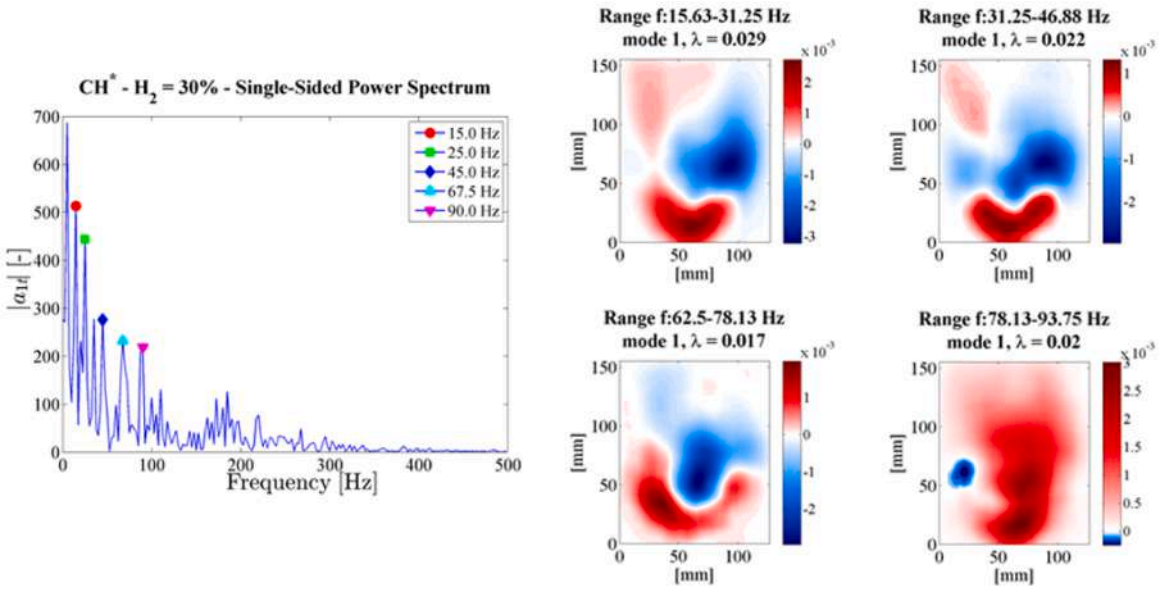


**Fig. 6.** FFT of the first mode extracted from the temporal coefficients of the POD (on the left) and flame structures of the first mode associated with frequency ranges selected through SPOD (on the right) - Chemiluminescence images of CH* with 30% $H_2$.

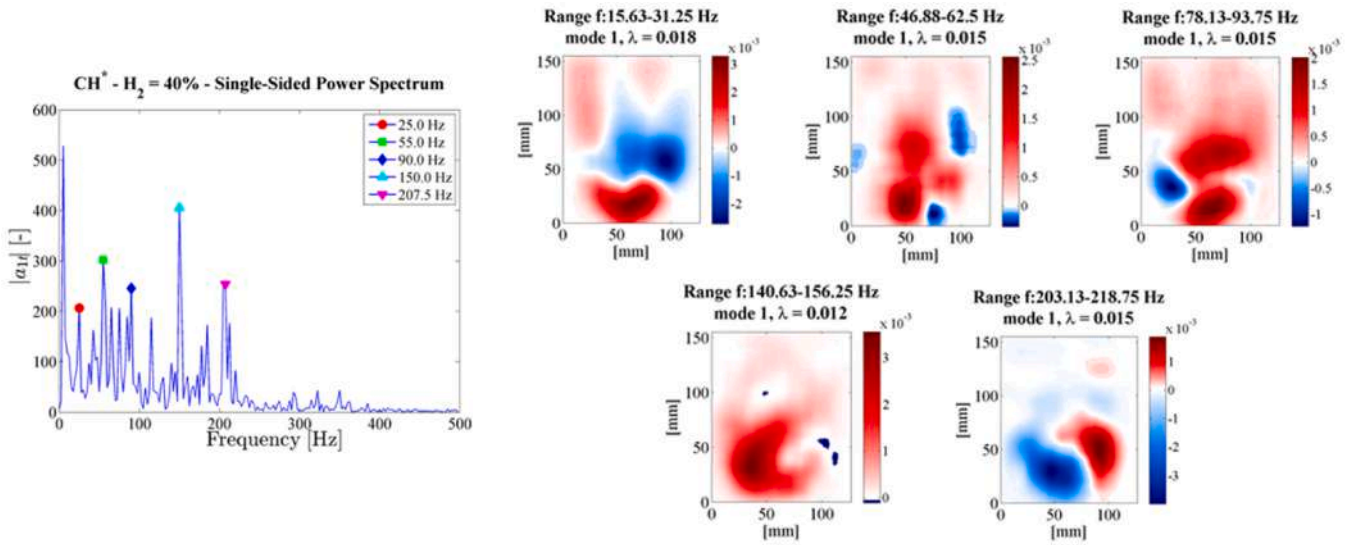


**Fig. 7.** FFT of the first mode extracted from the temporal coefficients of the POD (on the left) and flame structures of the first mode associated with frequency ranges selected through SPOD (on the right) - Chemiluminescence images of CH* with 40% $H_2$.

spectral density, as shown in Fig. 10, with peaks at 15, 20, 37.5, 75, 90, 150, and 207.5 Hz. The SPOD structures reveal longitudinal instabilities (15.63–31.25 Hz, $\lambda = 0.0039$), localized thermoacoustic gradients (31.25–46.88 Hz and 62.5–78.13 Hz), and amplified vortical modes (78.13–156.25 Hz). High-frequency structures in the 203.13–218.75 Hz range suggest direct coupling between unsteady heat release and the acoustic field. Nevertheless, the overall modal intensity remains relatively low, consistent with the more stable nature of the OH* signal, which represents advanced combustion zones and is less sensitive to unstable fluctuations.

To quantitatively assess the frequency-dependent dynamics of pressure oscillations and reactive species behavior under hydrogen-enriched conditions, a spectral energy integration was also performed. Using FFT amplitude spectra of pressure signals and the first POD mode amplitudes for CH* and OH* radicals, the normalized spectral energy was computed by integrating the squared amplitude over three frequency bands (0–150 Hz, 150–300 Hz, and 300–450 Hz) for hydrogen concentrations of 0%, 30%, and 40%. The resulting values are presented as bar charts grouped by species and frequency band. Comparison between the acoustic spectra and the CH*/OH* chemiluminescence response provides further insight into the flame–acoustic coupling. In the 0% $H_2$ case, although distinct pressure peaks are observed, the CH* and OH* dynamics are mainly governed by lower-frequency flame-structure fluctuations and do not exhibit a comparable broadening of the optical spectral content. This indicates that the pressure oscillations are only weakly associated with unsteady heat-release fluctuations. In contrast, hydrogen-enriched flames show both increased pressure amplitudes and broader, more fragmented CH*/OH* spectral structures, suggesting a stronger interaction between flame dynamics, heat-release fluctuations, and the acoustic field.

This integrated analysis (Fig. 11) enables a direct quantitative comparison across hydrogen concentrations. For the pressure signal,

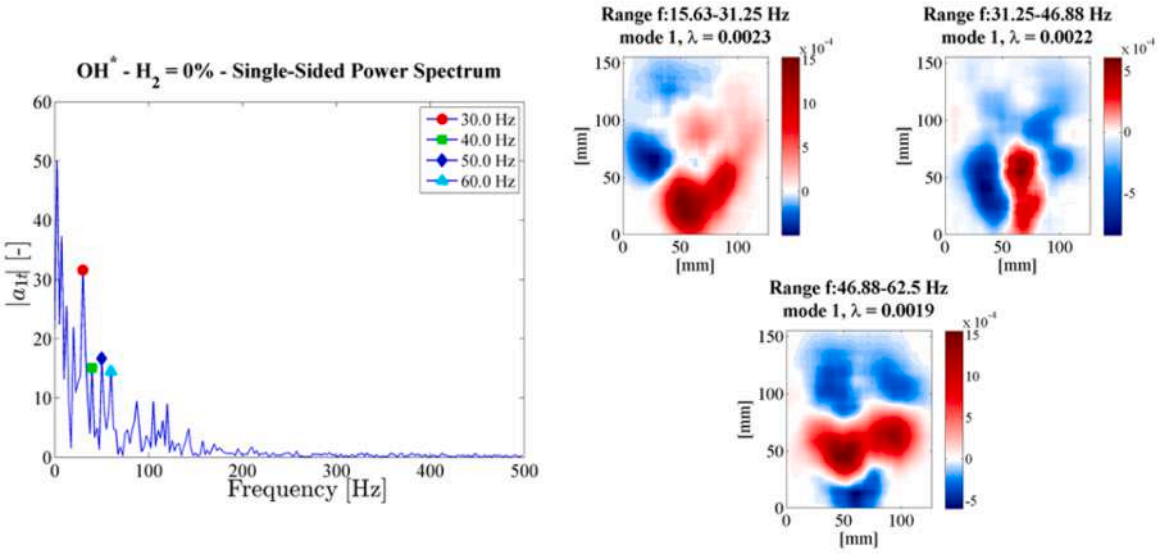


**Fig. 8.** FFT of the first mode extracted from the temporal coefficients of the POD (on the left) and flame structures of the first mode associated with frequency ranges selected through SPOD (on the right) - Chemiluminescence images of OH* with 0% $H_2$.

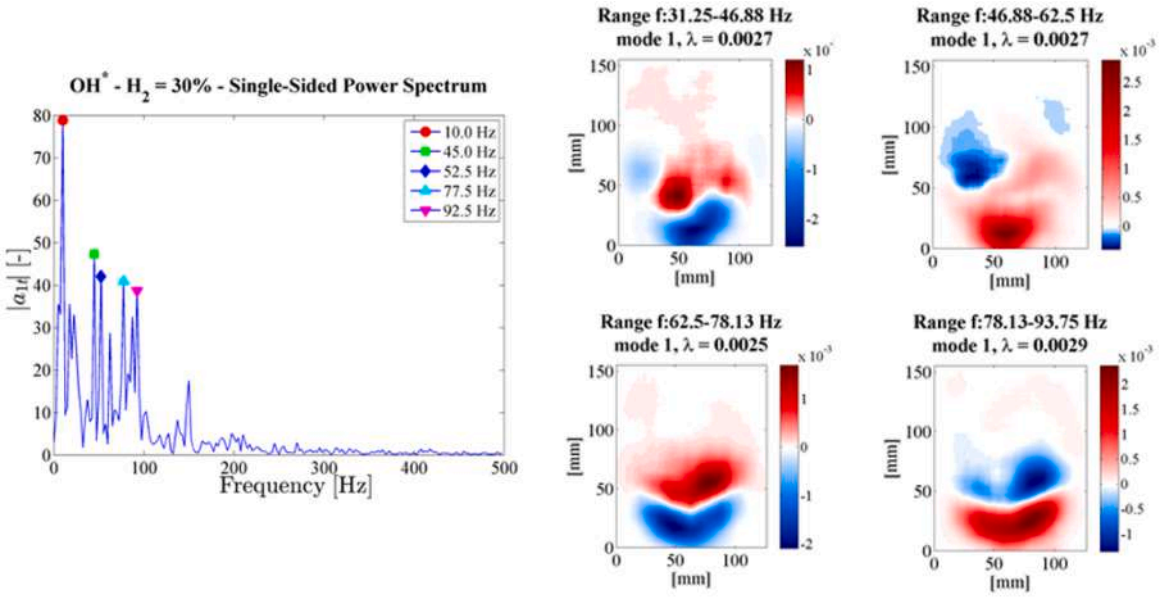


**Fig. 9.** FFT of the first mode extracted from the temporal coefficients of the POD (on the left) and flame structures of the first mode associated with frequency ranges selected through SPOD (on the right) - Chemiluminescence images of OH* with 30% $H_2$.

energy remains predominantly concentrated in the 150–300 Hz band, regardless of $H_2$ content, suggesting the persistence of acoustic modes and shear-layer instabilities that are relatively insensitive to changes in global reactivity. However, a reduction in low-frequency energy (0–150 Hz) is observed with increasing hydrogen fraction, likely reflecting diminished large-scale pressure fluctuations and a more compact flame structure. In contrast, the POD modes of CH* and OH*, which represent dominant flame-structure dynamics, show strong energy localization in the lowest frequency band (0–150 Hz), consistent with the slow evolution of coherent structures typical of premixed flames. In particular, the low-frequency OH* POD energy increases with hydrogen enrichment, indicating stronger modulation of the reaction zone. CH*, on the other hand, exhibits a non-monotonic trend, with a peak in mid-frequency energy (150–300 Hz) at 30% $H_2$, suggesting a regime characterized by intermittent flame features or localized extinction–reignition dynamics.

The broader spectral content observed at 40% $H_2$ for both radicals points to enhanced flame–turbulence interaction and the onset of thermo-diffusive instabilities. Hydrogen's high diffusivity and low Lewis number promote the development of smaller, rapidly evolving flame structures, increasing spectral energy over a wider frequency range and leading to a more complex and unsteady flame topology (Fig. 12).

To complement the primarily experimental investigation, one-dimensional laminar premixed flame simulations were carried out to provide theoretical insight into the effects of hydrogen enrichment on flame structure and transport properties. Simulations were performed using Cantera v3.1 in a freely propagating 1-D configuration at atmospheric pressure, with an unburned gas temperature Tu = 300 K and equivalence ratio $\phi = 0.80$. The fuel consisted of a binary $H_2/CH_4$ mixture with hydrogen mole fractions of 0%, 30%, and 40%. Chemical kinetics were modeled using GRI-Mech 3.0, with multicomponent transport under adiabatic, constant-pressure conditions. A 30 mm computational domain was discretized using adaptive mesh refinement,

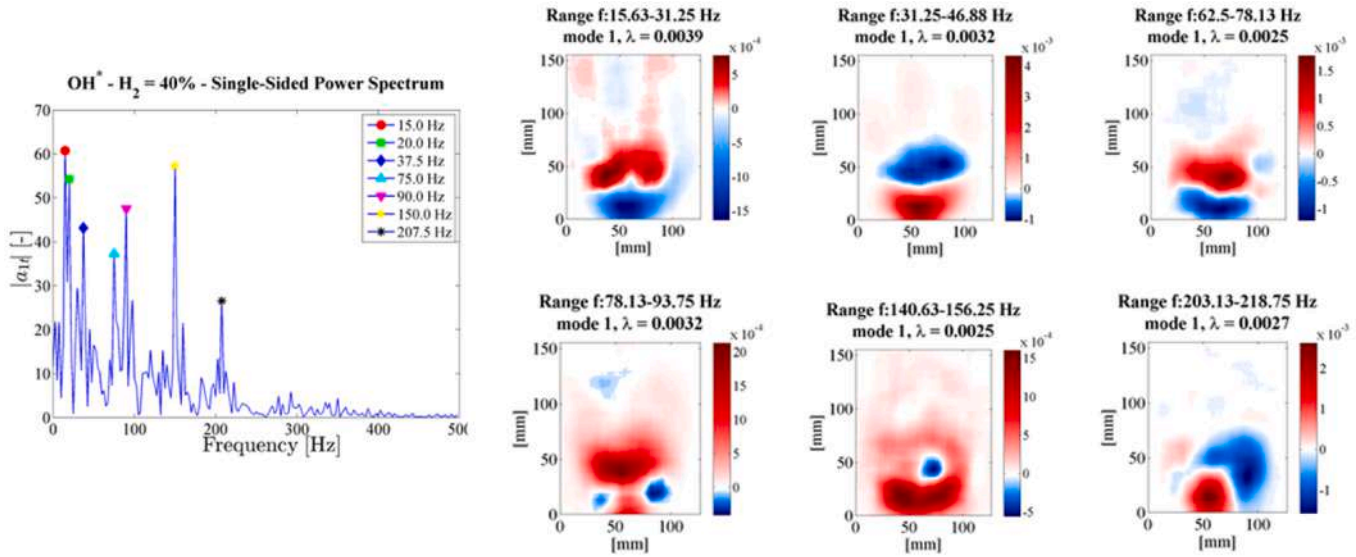


**Fig. 10.** FFT of the first mode extracted from the temporal coefficients of the POD (on the left) and flame structures of the first mode associated with frequency ranges selected through SPOD (on the right) - Chemiluminescence images of OH* with 40% $H_2$.

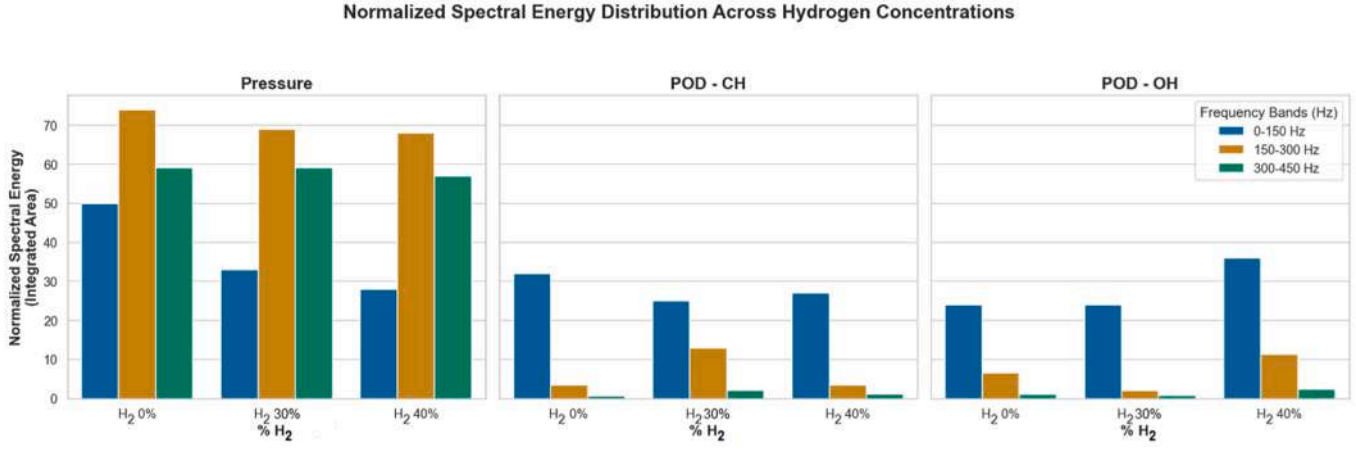


**Fig. 11.** Normalized spectral energy integrated over three frequency bands (0–150 Hz, 150–300 Hz, 300–450 Hz) for pressure and POD modes of CH and OH, at varying hydrogen concentrations (0%, 30%, 40%).

ensuring variations below 1% for key output quantities.

Although GRI-Mech 3.0 is not specifically optimized for pure hydrogen flames, the present simulations concern methane–hydrogen blends up to 40% $H_2$ by volume and are used to support the interpretation of global flame-structure trends rather than to provide mechanism-dependent quantitative predictions. In particular, the analysis focuses on laminar flame speed, reaction-zone thickness, heat-release localization, and Lewis-number-related effects. No quantitative conclusions on detailed hydrogen kinetics, pollutant formation, or pure hydrogen flame behavior are drawn from GRI-Mech 3.0 alone.

The heat-release rate was computed by summing the enthalpy-weighted net production rates of individual species. A chemiluminescence proxy was obtained by line-of-sight integration of OH and $CH_2O$ concentrations, providing a physically motivated estimate of radiative flame-front features. The reaction-zone thickness was estimated from the ratio of the temperature rise to the maximum temperature gradient, while the variance of the heat-release rate was calculated within the active flame region (>1% of the peak value). The Lewis number of hydrogen in the fresh gas was also evaluated as the ratio of thermal to mass diffusivity.

These calculated parameters consistently explain the experimentally observed effects of hydrogen enrichment. Increasing hydrogen fraction enhances the laminar flame speed and reduces reaction-zone thickness, leading to more concentrated heat-release profiles. The associated reduction in Lewis number promotes diffusive–thermal instabilities, increasing flame-front wrinkling and scalar fluctuation intensity, in agreement with the broader spectral features and higher variance detected in the FFT-based experimental analysis.

Hydrogen enrichment also intensifies the reactive zone and radical production, as evidenced by the monotonic increase of the chemiluminescence proxy $\int([OH]+[CH_2O])dz$ with increasing $H_2$ fraction. Numerically, this corresponds to progressively taller and narrower heat-release profiles, while the laminar flame speed $S_L$ increases and the flame thickness $\delta_L$ decreases, consistent with a faster and thinner flame front.

These numerical predictions directly correlate with experimental observations of more compact, intense, and highly variable CH* and OH* chemiluminescence fields. The increase in normalized heat-release variance with hydrogen enrichment supports the intensification of thermo-diffusive instabilities and explains the broadening of the acoustic spectrum and the emergence of high-frequency oscillatory modes, highlighting stronger coupling between unsteady heat release

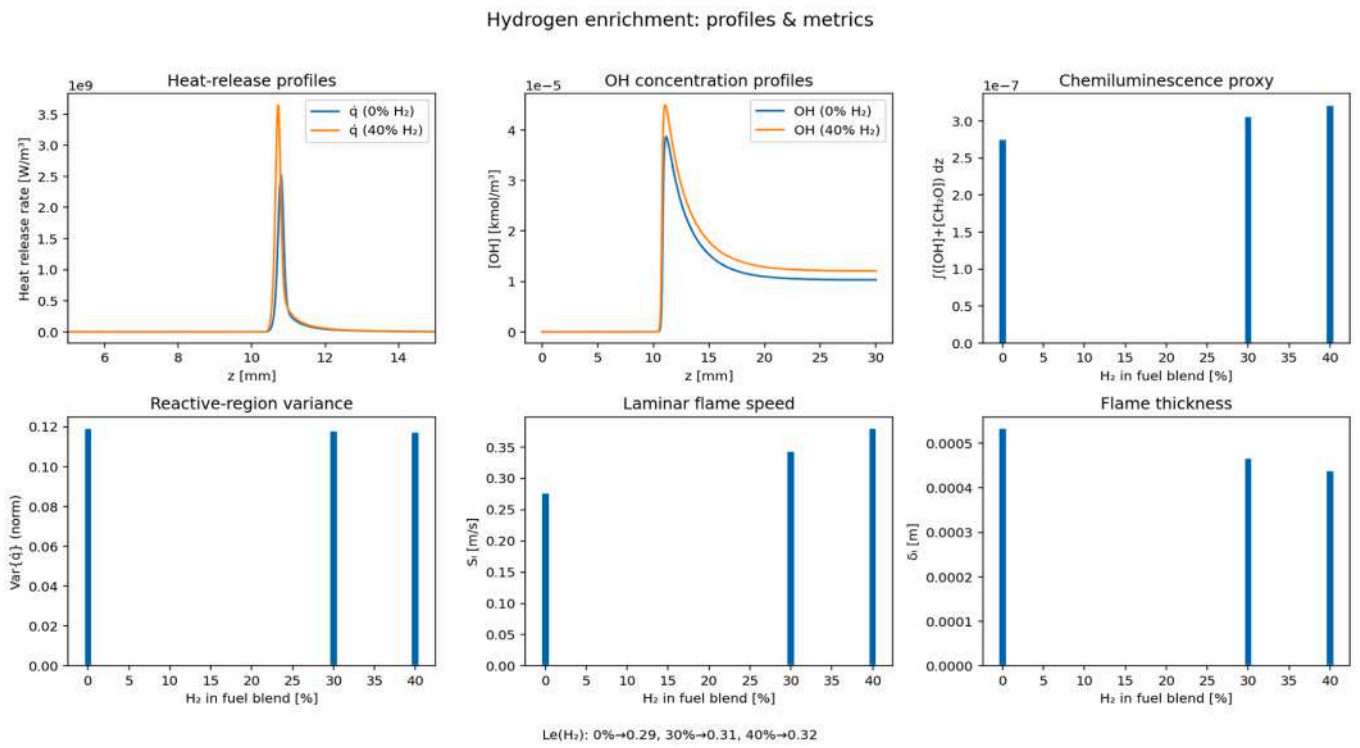


**Fig. 12.** Cantera results 1-D freely propagating premixed flames at 1 atm and temperature 300 K, F =0.80; and different $H_2/CH_4$ blends.

and the acoustic field. The hydrogen enrichment not only modifies flame structure by accelerating combustion and compressing the reaction zone, but also significantly increases the dynamic complexity of the system. The combined experimental and numerical analyses provide a robust mechanistic explanation for the observed increase in chemiluminescence intensity, fluctuation levels, and spectral richness, confirming the central role of hydrogen-induced thermo-diffusive and thermoacoustic effects in shaping flame dynamics.

### 3.3. *Autocorrelation function*

The autocorrelation function is a mathematical tool used to quantify

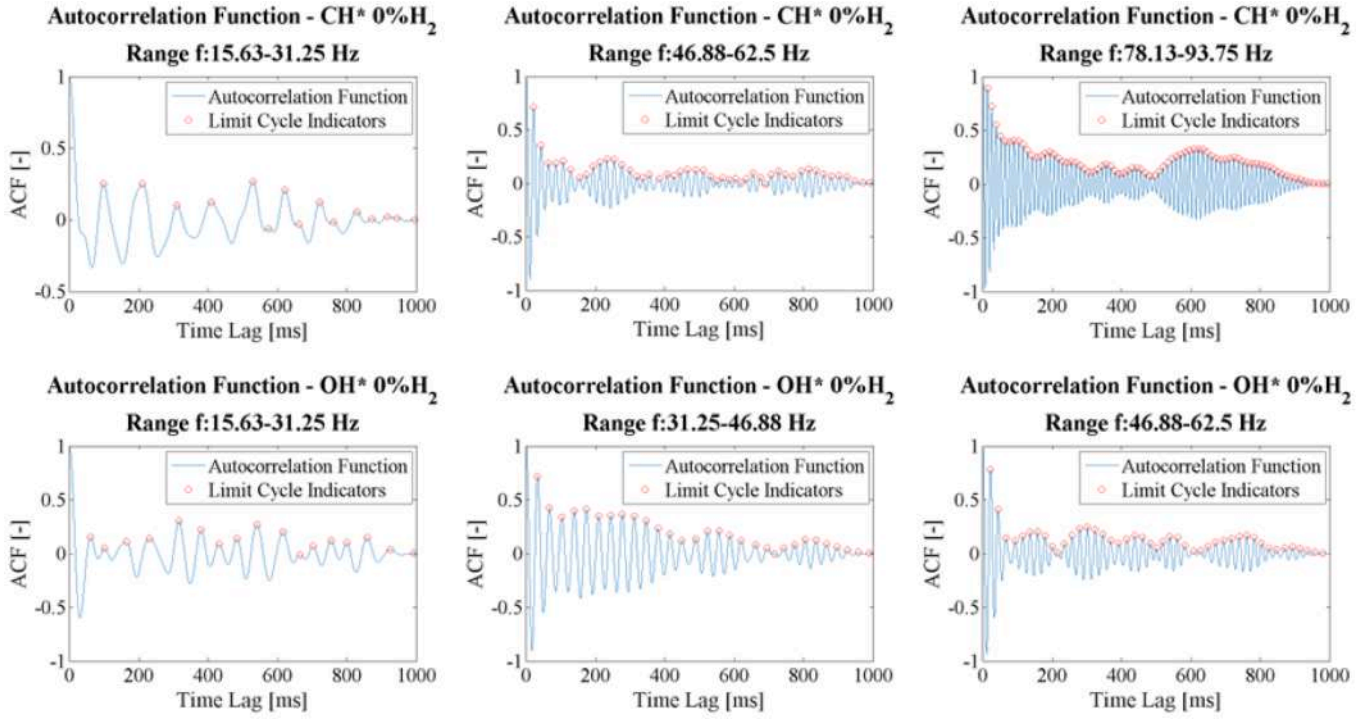


**Fig. 13.** Autocorrelation Function applied to the frequency ranges identified by SPOD for the 0% $H_2$ case; the top row refers to CH* chemiluminescence, the bottom row to OH* chemiluminescence.

the similarity of a signal with itself as a function of time delay. It enables the identification of periodicity, temporal coherence, and recurring behaviors within a time series [55]. In this study, the autocorrelation function was applied to signals projected onto the frequency bands selected via SPOD, allowing the assessment of the temporal persistence of oscillatory structures within each spectral interval [56,57].

For the case of pure methane combustion (0% $H_2$), the autocorrelation results are shown in Fig. 13, with CH* chemiluminescence signals in the top row and OH* in the bottom row. The CH* signal exhibits well-defined periodic oscillations with a slow amplitude decay, particularly in the 15.63–31.25 Hz band, indicating strong temporal coherence of heat-release fluctuations driven by hydrodynamic instabilities. At higher frequencies (46.88–62.5 Hz and 78.13–93.75 Hz), the autocorrelation decays more rapidly, suggesting transient flame dynamics and reduced persistence of the oscillatory structures. The OH* signal, representative of post-flame oxidation zones, shows a more damped response with lower amplitude, consistent with its reduced sensitivity to short-timescale fluctuations. Nevertheless, a residual low-frequency component (15.63–31.25 Hz) persists, indicating the presence of large-scale coherent motions even in the burned-gas region.

For the 30% $H_2$ methane–hydrogen blend (Fig. 14), the CH* autocorrelation reveals pronounced periodic components, with peaks persisting at long time delays. In the 31.25–46.88 Hz band, the function exhibits regular oscillations with slow decay, reflecting high temporal coherence and stable oscillatory structures over time. This behavior corresponds to enhanced hydrodynamic and thermoacoustic coupling due to the increased reactivity and heat-release rate of the mixture. Significant periodicity is also observed in the 62.5–78.13 Hz and 78.13–93.75 Hz bands, albeit with faster decay, indicating cyclic but less persistent dynamics. In the OH* domain, the response is more damped yet still displays cyclic behavior, particularly in the 31.25–46.88 Hz band, where distinct peaks indicate relatively regular post-flame fluctuations. At higher frequencies, the rapid decay suggests lower temporal coherence, likely associated with small-scale unstable phenomena.

For the 40% $H_2$ mixture (Fig. 15), both CH* and OH* autocorrelations decay rapidly and lose clear periodicity, signaling a breakdown of coherent structures. CH* displays irregular, weakly defined oscillations across all bands, indicative of a transition to turbulence-dominated, multi-frequency behavior. Similarly, OH* exhibits rapid decay and irregular patterns, with quasi-stochastic features in some bands, highlighting highly complex dynamics even in post-flame regions.

The evolution with increasing hydrogen fraction shows a transition from a stable, periodic hydrodynamic regime (0% $H_2$) to enhanced coherence in mid-frequency modes (30% $H_2$), and finally to chaotic, broadband fluctuations (40% $H_2$). This progression reflects the competing effects of hydrogen's high reactivity, which strengthens oscillatory coupling, and its high diffusivity, which promotes small-scale incoherent fluctuations. The autocorrelation function thus provides a robust quantitative indicator of the temporal persistence of thermoacoustic and hydrodynamic instabilities, clearly capturing the transition from coherent to intermittent and ultimately chaotic flame behavior as hydrogen content increases, consistent with SPOD observations and theoretical expectations for low-Lewis-number reactive mixtures.

## 4. CONCLUSION

The aerospace sector is increasingly adopting sustainable propulsion systems to reduce emissions and improve efficiency while maintaining performance, enabling quieter and more environmentally friendly aircraft.

A comprehensive experimental analysis was conducted to investigate the effects of hydrogen enrichment on premixed methane/air combustion in a swirl-stabilized burner operating at atmospheric pressure. The study employed high-speed chemiluminescence imaging, microphone-based pressure measurements, and advanced diagnostic techniques—including Zernike coefficients, Hu moments, Spectral Proper Orthogonal Decomposition (SPOD), and temporal autocorrelation—to examine the evolution of flame structure, stability, and dynamics as a function of hydrogen content.

Hydrogen addition was found to significantly alter flame morphology. At 30% and 40% $H_2$ by volume, CH* and OH* chemiluminescence emissions became more intense and spatially confined, indicating enhanced reaction rates and heat release. Morphological analysis showed a trend toward more compact and symmetric flame structures, characterized by reduced area, perimeter, and shape irregularity. These changes are consistent with the increased diffusivity, lower ignition energy, and faster kinetics associated with hydrogen. Despite improvements in flame reactivity, increased hydrogen levels also led to greater instability. Spectral analysis of microphone signals revealed amplified pressure oscillations in the 200–500 Hz range. At 30% $H_2$, dominant spectral peaks nearly doubled in amplitude compared to pure methane, while at 40% $H_2$, the spectral energy was redistributed and broadened, indicating a shift toward more chaotic combustion dynamics. SPOD analysis provided further insight, showing a transition

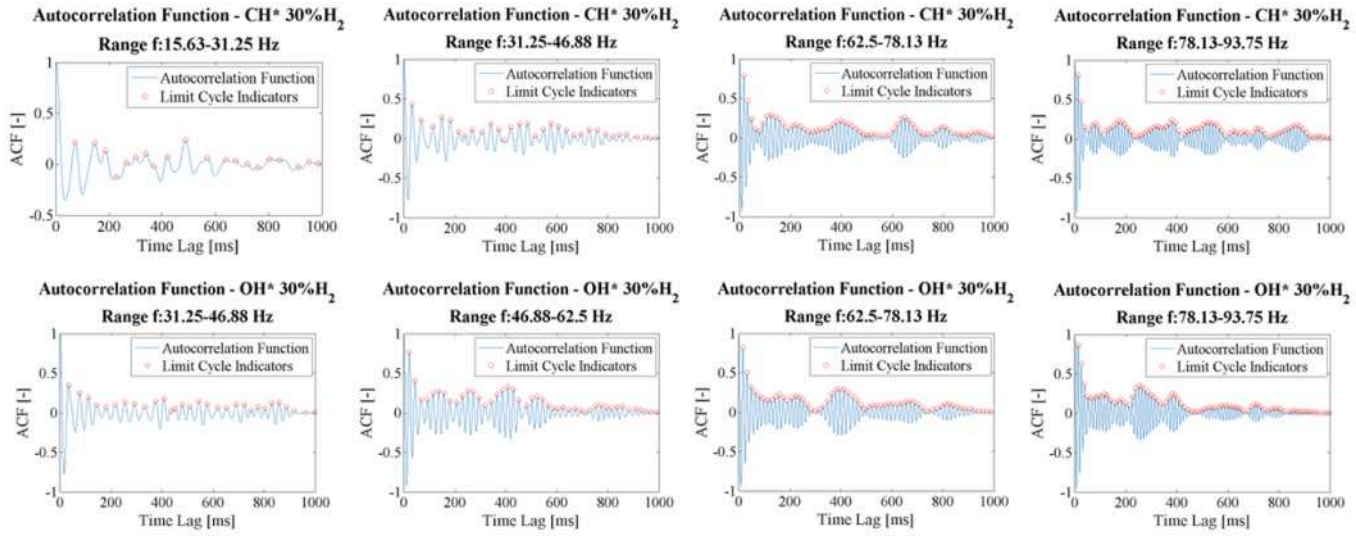


**Fig. 14.** Autocorrelation Function applied to the frequency ranges identified by SPOD for the 30% $H_2$ case; the top row refers to CH* chemiluminescence, the bottom row to OH* chemiluminescence.

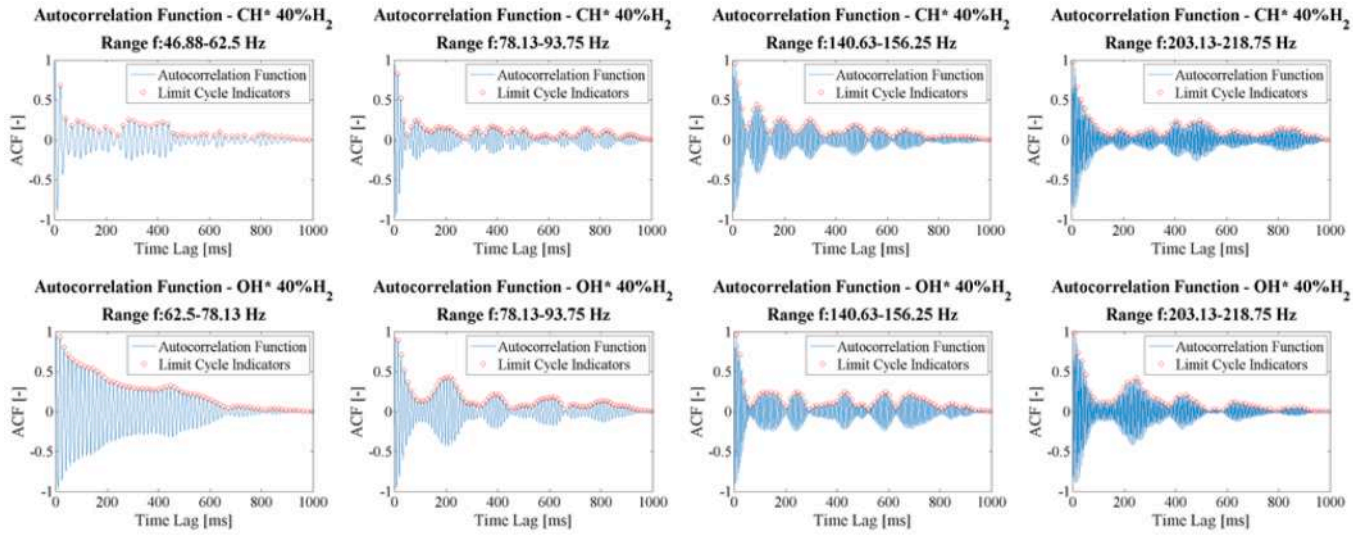


**Fig. 15.** Autocorrelation Function applied to the frequency ranges identified by SPOD for the 40% $H_2$ case; the top row refers to CH* chemiluminescence, the bottom row to OH* chemiluminescence.

from low-frequency, large-scale coherent modes at 0% $H_2$ to more complex, higher-frequency structures at elevated hydrogen levels. At 40% $H_2$, spatial modes appeared more fragmented and intermittent, reflecting a more turbulent and unstable regime.

Temporal autocorrelation analysis supported these findings, with stable, periodic oscillations observed at low hydrogen content and rapid signal decorrelation at higher concentrations, indicating reduced coherence and increased transient behavior. The combined application of spatial and temporal diagnostics enabled a detailed characterization of how hydrogen enrichment influences flame compactness and its susceptibility to thermoacoustic instabilities.

The present study focuses on flame dynamics and chemiluminescence-based diagnostics. Future investigations will address a finer hydrogen-enrichment resolution and the simultaneous characterization of pollutant emissions, including NOx and CO, to provide a more comprehensive assessment of hydrogen-enriched combustion systems.

The present study has several limitations that should be acknowledged. Only three hydrogen-enrichment levels were investigated, which limits the resolution of potential transition phenomena. The chemiluminescence acquisition frequency constrained the spectral analysis to frequencies below the Nyquist limit. Furthermore, pollutant emissions were not measured, and the one-dimensional numerical simulations based on GRI-Mech 3.0 were used primarily to support the interpretation of experimental trends. Future work will address these aspects through a broader parametric investigation, dedicated emissions measurements, and the application of kinetic mechanisms specifically developed for hydrogen-enriched combustion.

## CRediT authorship contribution statement

**Sara Bonuso:** Visualization, Formal analysis, Data curation. **Pasquale Di Gloria:** Validation, Software, Methodology. **Guido Marseglia:** Writing – review & editing, Writing – original draft, Investigation. **Maria Grazia De Giorgi:** Writing – original draft, Supervision, Resources, Project administration.

## Declaration of competing interest

The authors declare that they have no known competing financial interests or personal relationships that could have appeared to influence the work reported in this paper.

## Acknowledgements

The work was supported and funded by Project MOST Research Project: Sustainable Mobility Center (Centro Nazionale per la Mobilità Sostenibile—CNMS) CUP progetto: F83C22000720001; Codice del progetto:CN00000023. Additional funding was provided by the European Union through the call Project HORIZON FFLECS (Grant Agreement No.101096436 - CUP F83C23003480006) -"Novel Fuel-Flexible ultra-Low Emissions Combustion systems for Sustainable aviation - FFLECS".

## Data availability

Data will be made available on request.

## References

[1] S. Suo, F. Tian, L. Jiang, Y. Dai, M.O.A. Hamid, Y. Zhang, H. Qi, X. Yang, M. Xie, Investigation on premixed spherical hydrogen–air flame development, turbulence characteristics and NOx emission in porous media with different pellet sizes, Aerosp. Sci. Technol. 168 (2026) 111017, https://doi.org/10.1016/j.ast.2025.111017.

[2] B. Wang, T.Z. Jia, M. Zhao, Sustainable aviation fuels: key opportunities and challenges in lowering carbon emissions for aviation industry, Carbon Capture Sci. Technol. 13 (2024) 100263, https://doi.org/10.1016/j.ccst.2024.100263.

[3] R.A. Adjei, D. Xie, X. Ou, S. Li, Mission-adaptive energy management for hybrid-electric distributed propulsion aircraft with in-flight recharging and asymmetric regeneration, Aerosp. Sci. Technol. 176 (2026) 112078, https://doi.org/10.1016/j.ast.2026.112078.

[4] C. Li, Y. Zhao, X. Xu, J. Lu, M. Shan, Z. Tang, Combustion and emission investigation on a novel cavity-swirler-based aircraft combustor fueled by SAF and RP-3 kerosene, Aerosp. Sci. Technol. 168 (2026) 111099, https://doi.org/10.1016/j.ast.2025.111099.

[5] N. Ma, S.-W. Zhang, B.-G. Sun, L.-Z. Bao, Q.-H. Luo, Research on the development, adaptation and durability of a 140 kW aviation hydrogen internal combustion engine for general aviation, Aerosp. Sci. Technol. 175 (2026) 111961, https://doi.org/10.1016/j.ast.2026.111961.

[6] G. Jiang, M. Chen, H. Tang, J. Zhang, Influence of hydrogen fuel on the thermodynamic cycle and propulsive performance of aeroengines, Aerosp. Sci. Technol. 169 (2026) 111448, https://doi.org/10.1016/j.ast.2025.111448.

[7] N. Ma, Y.-L. Gao, B.-G. Sun, Q.-H. Luo, K. Chen, L.-Z. Bao, Co-optimization of dual spark plug ignition timing in a high-efficiency, low-emission hydrogen-fueled aviation engine, Aerosp. Sci. Technol. 177 (2026) 112312, https://doi.org/10.1016/j.ast.2026.112312.

[8] R. Xue, W. Gu, Q. Yang, X. Liu, X. Hui, Experimental investigation on combustion instability of hydrogen-enriched methane in a direct-injection swirl burner, Aerosp. Sci. Technol. 168 (2026) 110833, https://doi.org/10.1016/j.ast.2025.110833.

[9] B.-K. Sung, J.-E. Kim, E.-S. Lee, S.-M. Jeong, J.-Y. Choi, Flame structure and performance evaluation of rocket-type vitiated air heater with film cooling, Aerosp. Sci. Technol. 168 (2026) 111001, https://doi.org/10.1016/j.ast.2025.111001.

[10] J. Jiang, X. Zhang, T. Yu, B. Sun, H. Zhou, Z. Ren, Structural impact on flame dynamics and mode transition in dual-swirl hydrogen flames, Aerosp. Sci. Technol. 162 (2025) 110206, https://doi.org/10.1016/j.ast.2025.110206.

[11] J. Wang, X. Xue, X. Hui, S. Li, M. Han, Q. Xu, X. Deng, Flame structures and instability dynamics of sustainable aviation fuel in a staged combustor, Aerosp. Sci. Technol. 175 (2026) 111962, https://doi.org/10.1016/j.ast.2026.111962.

[12] J. Wu, Z. Huang, Continuously rotated upper wall on the flame dynamics and combustion performance of a model supersonic combustor, Aerosp. Sci. Technol. 171 (2026) 111627, https://doi.org/10.1016/j.ast.2026.111627.

[13] Y. Tian, Q. Luo, P. Wang, J. Nan, L. Yang, J. Li, Theoretical analysis on thermoacoustic dynamic responses of laminar premixed ammonia–hydrogen–air conical flames based on G-equation models, Aerosp. Sci. Technol. 164 (2025) 110398, https://doi.org/10.1016/j.ast.2025.110398.

[14] Y. Liu, Y. Zhang, X. Liu, Z. Liu, D. Che, Experimental and numerical investigation on premixed $H_2$/air combustion, Int. J. Hydrog. Energy 41 (2016) 10496–10506, https://doi.org/10.1016/j.ijhydene.2016.01.049.

[15] Jefferson Lab. Chapter 6 – flammability limits. In: flammable gas safety supplement, Available online, https://www.jlab.org/ehs/ehsmanual/FlamGas Supplement/FlamGas%20Ch6.htm, 2016. accessed 2 April 2026.

[16] G. Dahl, F. Suttrop, Engine control and low-NOx combustion for hydrogen fuelled aircraft gas turbines, Int. J. Hydrog. Energy 23 (1998) 695–704, https://doi.org/10.1016/S0360-3199(97)00115-8.

[17] H. Pan, S. Geng, H. Yang, G. Zhang, H. Bian, Y. Liu, Influence of $H_2$ blending on NOx production in natural gas combustion: mechanism comparison and reaction routes, Int. J. Hydrog. Energy 48 (2023) 784–797, https://doi.org/10.1016/j.ijhydene.2022.09.251.

[18] R. Xue, W. Gu, Q. Yang, X. Liu, X. Hui, Experimental investigation on combustion instability of hydrogen-enriched methane in a direct-injection swirl burner, Aerosp. Sci. Technol. 168 (2026) 110833, https://doi.org/10.1016/j.ast.2025.110833.

[19] S. Marragou, H. Magnes, T. Poinsot, L. Selle, T. Schuller, Stabilization regimes and pollutant emissions from a dual fuel $CH_4$/$H_2$ and dual swirl low NOx burner, Int. J. Hydrog. Energy 47 (2022) 19275–19288, https://doi.org/10.1016/j.ijhydene.2022.04.033.

[20] V. Patel, R. Shah, Effect of hydrogen enrichment on combustion characteristics of methane swirling and non-swirling inverse diffusion flame, Int. J. Hydrog. Energy 44 (2019) 28316–28329, https://doi.org/10.1016/j.ijhydene.2019.09.076.

[21] S. Kwak, J. Choi, M. Ahn, Y. Yoon, Effects of hydrogen addition on the forced response of $H_2$/$CH_4$ flames in a dual-nozzle swirl-stabilized combustor, Int. J. Hydrog. Energy 47 (2022) 28139–28151, https://doi.org/10.1016/j.ijhydene.2022.06.117.

[22] D. Li, R. Wang, G. Yang, J. Wan, Effect of hydrogen addition on the structure and stabilization of a micro-jet methane diffusion flame, Int. J. Hydrog. Energy 46 (2021) 5790–5798, https://doi.org/10.1016/j.ijhydene.2020.11.034.

[23] Q. An, et al., Flame stabilization mechanisms and shape transitions in a 3D printed hydrogen-enriched methane/air low-swirl burner, Int. J. Hydrog. Energy 46 (2021) 14764–14779, https://doi.org/10.1016/j.ijhydene.2021.01.112.

[24] S. Guo, J. Wang, W. Zhang, M. Zhang, Z. Huang, Effect of hydrogen enrichment on swirl/bluff-body lean premixed flame stabilization, Int. J. Hydrog. Energy 45 (2020) 10906–10919, https://doi.org/10.1016/j.ijhydene.2020.02.020.

[25] W. Wu, Y. Piao, H. Liu, Analysis of flame stabilization mechanism in a hydrogen-fueled reacting wall-jet flame, Int. J. Hydrog. Energy 44 (2019) 26609–26623, https://doi.org/10.1016/j.ijhydene.2019.08.073.

[26] H.S. Kim, V.K. Arghode, M.B. Linck, A.K. Gupta, Hydrogen addition effects in a confined swirl-stabilized methane–air flame, Int. J. Hydrog. Energy 34 (2009) 1054–1062, https://doi.org/10.1016/j.ijhydene.2008.10.034.

[27] M.E. Morsy, J. Yang, The instability of laminar methane/hydrogen/air flames: correlation between small and large-scale explosions, Int. J. Hydrog. Energy 47 (2022) 29959–29970, https://doi.org/10.1016/j.ijhydene.2022.06.289.

[28] H. Yilmaz, L. Schröder, T. Hillenbrand, D. Brüggemann, Effects of hydrogen addition on combustion and flame propagation characteristics of laser ignited methane/air mixtures, Int. J. Hydrog. Energy 48 (2023) 17324–17338, https://doi.org/10.1016/j.ijhydene.2023.01.2248.

[29] M. Reyes, R. Sastre, F.V. Tinaut, J. Rodríguez-Fernández, Study and characterization of the instabilities generated in expanding spherical flames of hydrogen/methane/air mixtures, Int. J. Hydrog. Energy 47 (2022) 22616–22632, https://doi.org/10.1016/j.ijhydene.2022.05.0632.

[30] Y. Xie, et al., Hydrogen addition effects on flame stability, Int. J. Hydrog. Energy 47 (2022) 35851–35863, https://doi.org/10.1016/j.ijhydene.2022.08.137.

[31] Castellani, et al., High-fidelity $H_2$–$CH_4$ jet in crossflow modelling with a flame index-controlled artificially thickened flame model, Int. J. Hydrog. Energy 48 (2023) 35291–35304, https://doi.org/10.1016/j.ijhydene.2023.05.210.

[32] J. Park, Y. Minamoto, M. Shimura, M. Tanahashi, Effects of hydrogen enrichment on $CH_4$/air turbulent swirling premixed flames in a cuboid combustor, Int. J. Hydrog. Energy 45 (2020) 9039–9051, https://doi.org/10.1016/j.ijhydene.2019.12.175.

[33] Y. Swarup, D. Jejurkar, P. Mishra, Flame stability studies in a hydrogen–air premixed flame annular microcombustor, Int. J. Hydrog. Energy 36 (2011) 7326–7338, https://doi.org/10.1016/j.ijhydene.2011.02.098.

[34] Z. Cai, X. Zhu, M. Sun, Z. Wang, Experiments on flame stabilization in a scramjet combustor with a rear-wall-expansion cavity, Int. J. Hydrog. Energy 42 (2017) 26752–26761, https://doi.org/10.1016/j.ijhydene.2017.09.059.

[35] L. Pachano, A. Surapaneni, A. Both, H. Ax, N. Petry, I. Boxx, D. Mira, Numerical assessment of the effect of hydrogen enrichment of a technically premixed swirl-stabilized natural gas flame, in: Proceedings of the ASME Turbo Expo, GT2023-102634, 2023, https://doi.org/10.1115/GT2023-102634.

[36] P. Kasabov, N. Zarzalis, P. Habisreuther, Experimental study on lifted flames operated with liquid kerosene at elevated pressure and stabilized by outer recirculation, Flow. Turbul. Combust. 90 (2013) 605–619, https://doi.org/10.1007/s10494-013-9444-1.

[37] Z. Zhou, et al., Quantitative measurement of OH and CH chemiluminescence, ACS. Omega 5 (2020) 15922–15930, https://doi.org/10.1021/acsomega.0c01093.

[38] T. Paschal, et al., High-speed OH and CH chemiluminescence imaging and OH* PLIF in spherically expanding flames, in: AIAA SciTech, 2019, https://doi.org/10.2514/6.2019-0574.

[39] S.X. Liao, M. Pawlak, On image analysis by moments, IEEE Trans. Pattern. Anal. Mach. Intell. 18 (1996) 254–266, https://doi.org/10.1109/34.485554.

[40] W.Y. Kim, Y.S. Kim, Region-based shape descriptor using Zernike moments, Signal Process.: Image Commun. 16 (2000) 95–102, https://doi.org/10.1016/S0923-5965(00)00019-9.

[41] M.K. Hu, Visual pattern recognition by moment invariants, IRE Trans. Inf. Theory 8 (1962) 179–187, https://doi.org/10.1109/TIT.1962.1057692.

[42] J. Flusser, T. Suk, Rotation moment invariants for recognition of symmetric objects, IEEE Trans. Image Process. 15 (2006) 3736–3745, https://doi.org/10.1109/TIP.2006.881969.

[43] A. Towne, et al., Spectral proper orthogonal decomposition and its relationship to DMD and resolvent analysis, J. Fluid. Mech. 847 (2018) 821–867, https://doi.org/10.1017/jfm.2018.283.

[44] P.D. Welch, The use of FFT for estimation of power spectra, IEEE Trans. Audio Electroacoust. 15 (1967) 70–73, https://doi.org/10.1109/TAU.1967.1161901.

[45] M. Sieber, K. Oberleithner, C.O. Paschereit Spectral proper orthogonal decomposition. arXiv preprint (2015), arXiv:1508.04642.

[46] T. Chu, O.T. Schmidt A stochastic SPOD-Galerkin model for broadband turbulent flows. arXiv preprint (2020), arXiv:2012.02902.

[47] P.D. Welch, The use of fast fourier transform for the estimation of power spectra: a method based on time averaging over short, modified periodograms, IEEE Trans. Audio Electroacoust. 15 (1967) 70–73, https://doi.org/10.1109/TAU.1967.1161901.

[48] A.P. Dowling, S.R. Stow, Acoustic analysis of gas turbine combustors, J. Propuls. Power. 19 (2003) 751–764, https://doi.org/10.2514/2.6192.

[49] T.C. Lieuwen, V. Yang, Combustion instabilities in gas turbine engines: operational experience, fundamental mechanisms, and modeling, Prog. Astronaut. Aeronaut. 210 (2005). AIAA.

[50] P. Di Gloria, M.G. De Giorgi, L. Strafella, G. Ciccarella, G.G. Castelluzzo, F. Baldassarre, A. Ficarella, Advancements in sustainable aviation fuels: impact of nano-additives and ammonia-based strategies on emissions, in: Proceedings of the ASME Turbo Expo, GT2024-128827, 2024, https://doi.org/10.1115/GT2024-128827.

[51] B.M. Zhang, M. Shahsavari, B.C. Wang, et al., Contributions of hydrodynamic features of a swirling flow to thermoacoustic instabilities in a lean premixed swirl stabilized combustor, Phys. Fluids 31 (2019) 075106, https://doi.org/10.1063/1.5108856.

[52] D. Fritsche, M. Füri, K. Boulouchos, An experimental investigation of thermoacoustic instabilities in a premixed swirl-stabilized flame, Combust. Flame 151 (1–2) (2007) 29–36, https://doi.org/10.1016/j.combustflame.2007.05.012.

[53] M. Stöhr, I. Boxx, C.D. Carter, W. Meier, Detailed characterization of the dynamics of thermoacoustic pulsations in a lean premixed swirl flame, Combust. Flame 150 (1–2) (2007) 2–26, https://doi.org/10.1016/j.combustflame.2007.04.002.

[54] A.D. Kumar, J.C. Massey, I. Boxx, N. Swaminathan, Effects of hydrogen enrichment on thermoacoustic and helical instabilities in swirl stabilised partially premixed flames, Flow. Turbul. Combust. 112 (2024) 689–727, https://doi.org/10.1007/s10494-023-00504-4.

[55] M.G. De Giorgi, P. Di Gloria, D. Fontanarosa, A. Ficarella, Advanced multiscale modal and frequency analysis of swirling spray flame near to lean blowout, Case Stud. Therm. Eng. 60 (2024) 104651, https://doi.org/10.1016/j.csite.2024.104651.

[56] K. Taira, S.L. Brunton, S.T.M. Dawson, C.W. Rowley, T. Colonius, B.J. McKeon, O. T. Schmidt, S. Gordeyev, V. Theofilis, L.S. Ukeiley, Modal analysis of fluid flows: an overview, AIAA J. 55 (2017) 4013–4041, https://doi.org/10.2514/1.J056060.

[57] S. Candel, D. Durox, T. Schuller, J.-F. Bourgouin, J.P. Moeck, Dynamics of swirling flames, Annu Rev. Fluid. Mech. 46 (2014) 147–173, https://doi.org/10.1146/annurev-fluid-010313-141300.